



Concept Definition Study for In-Space Structural Characterization of a Lightweight Solar Array: Final Report

*Jessica A. Woods-Vedeler, Richard S. Pappa, Thomas W. Jones, Regina Spellman, and Willis Scott
Langley Research Center, Hampton, Virginia*

*Eric M. Mockensturm
Pennsylvania State University, University Park, Pennsylvania*

*Donn Liddle, Ed Oshel, and Michael Snyder
Johnson Space Flight Center, Houston, Texas*

The NASA STI Program Office . . . in Profile

Since its founding, NASA has been dedicated to the advancement of aeronautics and space science. The NASA Scientific and Technical Information (STI) Program Office plays a key part in helping NASA maintain this important role.

The NASA STI Program Office is operated by Langley Research Center, the lead center for NASA's scientific and technical information. The NASA STI Program Office provides access to the NASA STI Database, the largest collection of aeronautical and space science STI in the world. The Program Office is also NASA's institutional mechanism for disseminating the results of its research and development activities. These results are published by NASA in the NASA STI Report Series, which includes the following report types:

- **TECHNICAL PUBLICATION.** Reports of completed research or a major significant phase of research that present the results of NASA programs and include extensive data or theoretical analysis. Includes compilations of significant scientific and technical data and information deemed to be of continuing reference value. NASA counterpart of peer-reviewed formal professional papers, but having less stringent limitations on manuscript length and extent of graphic presentations.
- **TECHNICAL MEMORANDUM.** Scientific and technical findings that are preliminary or of specialized interest, e.g., quick release reports, working papers, and bibliographies that contain minimal annotation. Does not contain extensive analysis.
- **CONTRACTOR REPORT.** Scientific and technical findings by NASA-sponsored contractors and grantees.
- **CONFERENCE PUBLICATION.** Collected papers from scientific and technical conferences, symposia, seminars, or other meetings sponsored or co-sponsored by NASA.
- **SPECIAL PUBLICATION.** Scientific, technical, or historical information from NASA programs, projects, and missions, often concerned with subjects having substantial public interest.
- **TECHNICAL TRANSLATION.** English-language translations of foreign scientific and technical material pertinent to NASA's mission.

Specialized services that complement the STI Program Office's diverse offerings include creating custom thesauri, building customized databases, organizing and publishing research results . . . even providing videos.

For more information about the NASA STI Program Office, see the following:

- Access the NASA STI Program Home Page at <http://www.sti.nasa.gov>
- Email your question via the Internet to help@sti.nasa.gov
- Fax your question to the NASA STI Help Desk at (301) 621-0134
- Telephone the NASA STI Help Desk at (301) 621-0390
- Write to:
NASA STI Help Desk
NASA Center for AeroSpace Information
7121 Standard Drive
Hanover, MD 21076-1320

NASA/TM-2002-211629



Concept Definition Study for In-Space Structural Characterization of a Lightweight Solar Array: Final Report

*Jessica A. Woods-Vedeler, Richard S. Pappa, Thomas W. Jones, Regina Spellman, and Willis Scott
Langley Research Center, Hampton, Virginia*

*Eric M. Mockensturm
Pennsylvania State University, University Park, Pennsylvania*

*Donn Liddle, Ed Oshel, and Michael Snyder
Johnson Space Flight Center, Houston, Texas*

National Aeronautics and
Space Administration

Langley Research Center
Hampton, Virginia 23681-2199

March 2002

The use of trademarks or names of manufacturers in this report is for accurate reporting and does not constitute an official endorsement, either expressed or implied, of such products or manufacturers by the National Aeronautics and Space Administration.

Available from:

NASA Center for AeroSpace Information (CASI)
7121 Standard Drive
Hanover, MD 21076-1320
(301) 621-0390

National Technical Information Service (NTIS)
5285 Port Royal Road
Springfield, VA 22161-2171
(703) 605-6000

Concept Definition Study for In-Space Structural Characterization of a Lightweight Solar Array: Final Report

**Jessica A. Woods-Vedeler, Richard S. Pappa
Thomas W. Jones, Regina Spellman and Willis Scott**
NASA Langley Research Center
Hampton, VA

Eric M. Mockensturm
Department of Mechanical and
Nuclear Engineering
Pennsylvania State University

Donn Liddle, Ed Oshel, Michael Snyder
Image Science and Analysis Group
NASA Johnson Space Flight Center
Houston, Texas

Abstract

A Concept Definition Study (CDS) was conducted to develop a proposed "Lightweight High-Voltage Stretched-Lens Concentrator Solar Array Experiment" under NASA's New Millennium Program Space Technology-6 (NMP ST-6) activity. As part of a multi-organizational team, NASA Langley Research Center's (LaRC) role in this proposed experiment was to lead Structural Characterization of the solar array during the flight experiment. In support of this role, NASA LaRC participated in the CDS to define an experiment for static, dynamic and deployment characterization of the array. In this study, NASA LaRC traded state-of-the-art measurement approaches appropriate for an in-space, STS-based flight experiment, provided initial analysis and testing of the lightweight solar array and lens elements, performed a lighting and photogrammetric simulation in conjunction with JSC and produced an experiment concept definition to meet structural characterization requirements.

Introduction

NASA Langley Research Center (LaRC) partnered with AEC-Able (industry lead), ENTECH, ILC Dover, NASA Marshall Spaceflight Center (MSFC), NASA Glenn Research Center (GRC) and Auburn Space Power Institute in the Fall of 2000 to propose the flight demonstration of a Gossamer solar array. In February, 2001, NASA's New Millennium Program Space Technology-6 (NMP ST-6) office awarded funding for a 6-month Concept Definition Study (CDS) to further develop the proposed "Lightweight High-Voltage Stretched-Lens Concentrator Solar Array Experiment". NASA Langley Research Center's (LaRC) role in this proposed experiment was to lead Structural Characterization of the solar array during the flight experiment. In support of this role, LaRC participated in the CDS to define an experiment for static, dynamic and deployment characterization of the array.

NASA LaRC has participated in two similar experiments in the past: the Solar Array Flight Experiment (SAFE)¹ on STS-41D in 1984 and the Photogrammetric Appendage Structural Dynamics Experiment (PASDE)² on STS-74 in 1995. In SAFE, a 105 ft long solar array was deployed from the shuttle payload bay and consisted of 84 panels made of 3-mil thick Kapton. NASA LaRC's role in the NASA MSFC-led mission was to investigate the structural dynamics and control of a new class of light-weight, low frequency space structures and to develop remote video measurement techniques to characterize structural dynamic performance on orbit. In this experiment, LaRC researchers were able to measure the 3.5% first-mode damping of the array, to measure thermally induced static shape distortion and to observe residual steady-state motion of the array. The NASA LaRC-led PASDE experiment was an International Space Station (ISS) risk mitigation experiment for a photogrammetric approach to monitor the dynamics of ISS appendages. In this experiment, video cameras were flown in shuttle-based Hitchhiker³ canisters and were used to measure dynamic motion of a MIR solar array. In contrast to SAFE, this experiment used elements of the natural scene as photogrammetric features. No

measurement 'targets' were placed apriori. Three bending modes and two system modes involving the Space Shuttle and Mir were identified using photogrammetry during this experiment.

In the current study, NASA LaRC performed analysis and testing in support of its role on the team. After a brief experiment overview, the results of this work will be presented. This includes results from a trade study to compare state-of-the-art structural measurement approaches appropriate for an in-space, STS-based flight experiment; initial structural analysis and testing of the lightweight solar array and lens elements; a lighting and photogrammetric simulation in conjunction with JSC; and an experiment concept definition to meet the structural measurement requirements.

Experiment Overview

The focus of this experiment is a lightweight, deployable solar array. A concept of the array experiment is shown in Figure 1⁴. The array is composed of 8, 1-meter long panels that are deployable from a stowed position. Each panel is composed of several key sub-components, enabling this concept to be a revolutionary advance beyond current solar array technology.

The most apparent of these sub-components is a novel concept used to focus incident solar radiation onto a 1-cm wide line of highly efficient solar cells^{5,6,7}. The focusing lens is a tensioned Fresnel lens made of flight qualified silicon material. A photo of the membrane lens is shown in Figure 2. The figure shows a demonstration article manufactured by ENTECH, an NMP ST-6 partner. In the flight test article, elements such as this would be 1 meter long and 9 cm wide. They would be placed side by side to fill an entire 3 meter wide array panel and tensioned at an appropriate level to maintain desired lens curvature.

Light from the Fresnel lens is focused onto highly efficient, triple junction solar cells⁸. A triple junction cell is composed of three layers of material. Each layer converts a different bandwidth of incident solar energy to electrical energy and transmits at other wavelengths. For this experiment, the top junction is GaInP, which converts wavelengths from about 0.36 to 0.7 microns. GaAs is the second junction, which converts wavelengths from about 0.6 - 0.9 microns. The bottom junction is Ge, which converts wavelengths from about 0.9 - 1.8 microns. Overall, ENTECH's current cells convert incident radiation to power with a 30-32% efficiency. As a reference, the International Space Station (ISS) arrays operate at about 10% efficiency.

All these components are mounted to a stiff backing that acts as a thermal radiator for the array. This backing is a very thin and lightweight composite material having a 90 degree weave of high thermal conductivity carbon fibers that are cured with a cyanate resin to make it rigid.

In addition, the array is sized to demonstrate performance as required under the New Millennium Program's (NMP) ST-6 and as listed in Table 1⁹. It is noted that for this demonstration, the array is not likely to be fully populated with lenses and solar cells to keep costs down, but the performance will be scalable. Table 2 lists upper level design requirements for the proposed experiment.

Finally, the platform for this proposed experiment is the roof-top of a Space Hab Research Module. Figure 3 shows the SpaceHab Single Module placement for a typical mission⁴. The lightweight solar array would be deployed from the roof-top of such a module. It could then be rotated axially 360 degrees on a slip ring for solar tracking purposes or for structural characterization.

Measurement Objectives

The structural measurement objectives include shape and vibration measurements of the array-level (Global) behavior and the stretched lens (Local) behavior. In particular, deployment dynamics, static shape and vibration modes of the array and lens must be measured.

Monitoring and characterizing the global dynamics of a deploying gossamer structure is of importance because it is during the deployment period that unanticipated motions or constraints can cause damage to critical spacecraft elements such as the solar array. Being able to validate models of nominal deployment performance aids in reducing risk associated with such deployment. Having such capability is particularly valuable for the

much larger (20-40 meter) gossamer structures envisioned for the future whose deployment can not easily be tested on the ground.

The global static shape measurement is critical for correlation with solar array performance. For the proposed solar array, sun pointing must be maintained to within about 2.5 degrees to maximize power collection. At higher pointing angles, power is significantly reduced due to the solar array optical geometry. As such, it is advantageous to acquire data at various thermal conditions such as daytime and nighttime when the highest and lowest steady state temperatures occur and during the day-night transition when thermal transients may induce shape distortion or structural motion.

Dynamic characterization of the array and individual lenses is important for several reasons as well. Obviously, measuring global dynamic behavior of the array is of immediate importance for structural model validation and monitoring during the experiment. However, demonstrating the ability to measure the local dynamics of individual lenses is of much greater significance for future gossamer space-structure applications and represents a key challenge of this experiment. Due to the low mass and high reflectivity of these lenses, such measurements are difficult using traditional in-situ sensor or optical methods. The dynamics are also difficult to predict due to a strong variability of natural frequency with in-plane tension. Such tension variations can occur in space due to thermal variations, the absence of gravity or imperfections in the deployed shape of the lens. Thus, successful experimental characterization of the local lens dynamic behavior represents a step-forward in the ability to characterize lightweight gossamer materials for many other space structure applications.

Finally, in order to obtain adequate information to derive the first few mode shapes of the array, it is desirable to obtain measurements with at least 1:3000 accuracy. This corresponds to less than 1 mm on the 3-meter wide structure.

Photogrammetric Measurement System Analysis

Trade-Study on Measurement Approach

In order to define the optimal measurement approach for a shuttle-based system, currently available photogrammetric systems were evaluated. In this trade-study, numerous systems were identified and compared.

In particular, the standard Space-Shuttle cargo bay video cameras, LaRC supplied high accuracy metrology camera systems, the JSC/Sandia Laser Dynamic Range Imager (LDRI), the Canadian Space Agency's Laser Camera System, Laser Doppler Vibrometry, Structured Light Techniques, Active Targets and others were considered. While each system offered advantages and disadvantages, the main criterion for comparison was the instrument flight-readiness, mass and cost to re-fly.

Tables 3 and 4 summarizes selection criteria for the top four systems considered. Table 3 includes measurement system hardware specifications and Table 4 shows measurement system operational specifications. The first three systems indicated have been or were flight ready at the time of the study. PASDE-lite was a lighter weight system concept developed based on the PASDE heritage but not yet built.

Operational lighting conditions were a significant consideration for this experiment. For instance, the LDRI is a system that operates only at night due to the low intensity infrared laser light used for measurements. Thus, static shape and dynamic motion would have to be measured at night. However, it was desirable to make dynamic measurements during solar tracking events to correlate with solar cell power measurements or during day-night transitions to measure thermally induced motion.

The added weight of each of these systems was also an important selection criteria due to the impact on overall system cost for a SpaceHab based experiment. The added weight varied from zero to about 25 lbs, not including data acquisition hardware that was estimated to be at least 40 lbs.

Ultimately, the space shuttle cameras were selected as the most cost-effective system to use although they are not specifically designed for such metrology and provide less-than-ideal accuracy when used in a photogrammetric capacity. As an additional option to this baseline concept, the use of LaRC provided, high accuracy mini-cameras located under individual lens elements was proposed.

Photogrammetric Angle and Accuracy Analysis

In order to get an initial, quantitative assessment of the suitability of space shuttle cameras for this application, a photogrammetric simulation was performed¹⁰. The objective was to identify optimal positions and accuracy of shuttle cameras for photogrammetric measurements of the array and lenses to determine if measurement requirements could be met.

The suitability of cameras for use in photogrammetric analysis is gauged by the predicted accuracy of the resulting measurements. The most significant factors controlling photogrammetric accuracy are the image resolution, camera geometry relative to the object, accuracy of the image measurements, and, in some cases, how accurately the photogrammetric solution reestablishes the absolute object coordinate system.

For this experiment, the shuttle Color Television Cameras (CTVC) were proposed and one is shown in Figure 4. They are 3-CCD chip broadcast quality cameras with a variable zoom range of 10 to 74 degrees Horizontal Field of View (HFOV). Each camera is equipped with a Light Emitting Diode (LED) light ring (the speckled blue area in Figure 4 surrounding the lens) which provides about 80 feet of illumination for possible nighttime measurements. The cameras are mounted on pan and tilt units that can be used by the crew or ground controllers to manipulate the camera's pointing angle.

Possible camera mounting locations in the shuttle payload bay are shown in Figure 5. There are two locations on the forward bulkhead and two on the aft bulkhead. When the Remote Manipulator Arm (RMA) is flown, an additional camera is located at the arm's elbow giving an additional viewing location from the shuttle's port side. It is also assumed that the solar array is mounted on top of SpaceHab as shown previously in Figure 3.

Using the camera and geometry information, simulated camera views were generated to evaluate the image accuracies. The simulation used an AEC-Able provided Pro-Engineer¹¹ model of the lightweight solar array and a similar model for the space shuttle and SpaceHab research module. Camera views from the five different shuttle camera locations could be generated. Typical simulated views are shown in Figure 6. In this case, the array is located on the starboard side of SpaceHab and the plane of the array is oriented parallel to the shuttle X-axis.

Intersection angles were then calculated using pairs of the simulated images. A nominal range of intersection angles between two camera views was between 45 and 140 degrees with the optimal intersection angle at about 110 degrees. Angle intersections less than 30 degrees or more than 150 degrees were considered to be unusable.

An accuracy assessment was next performed. Numbers presented in this study are the axial dimensions of an "uncertainty volume." This volume is computed by intersecting a theoretical conical structure from each camera to the object point. The included angle of each camera's cone is controlled by the camera focal length, the image measurement uncertainty and the camera-to-object distance. For all accuracy estimates presented in this study, the image resolution is held constant at 640 x 480 pixels and the image measurement uncertainty set at a conservative value of 1/3rd of a pixel. It is noted that the axial dimensions of the "uncertainty volume" are not relative to any measurement or object coordinate system, but rather solely to the volume itself.

The angle and accuracy assessments were performed for four operational scenarios that included measuring array deployment, static shape, global array-level dynamic response and local lens dynamic response. For each scenario, different paired combinations of the five shuttle cameras were considered relative to three points on the array located at the top, middle and bottom of the array's vertical axis.

Array Deployment

During deployment, full array coverage was required to document the 3-dimensional motion of the array. To provide this capability, each camera pair had to be able to view the complete solar array from a single orientation. The array plane was assumed to be parallel with the shuttle X-axis.

Table 5 summarizes results of the angle assessment. Two locations of the array are considered on the starboard and port side of the SpaceHab rooftop. Dark shaded blocks indicate unacceptable intersection angles

for each camera pair. Cross-hatched blocks indicate acceptable but undesirable intersection angles. Table 6 summarizes results of the accuracy assessment for camera pairs with acceptable intersection angles. Minimum dimensions of the uncertainty volume are desirable.

These results show that the "B-Elbow" camera pair provides the highest accuracy and meets the measurement requirement during deployment whether the array is mounted on the port or starboard side of SpaceHab. If the elbow camera is not available or is being used for close-up views, camera pair "C-D" is acceptable if the array is on the port side of SpaceHab or pair "A-B" if the array is on the starboard side.

Viewing simulations from the "B-Elbow" cameras were shown in Figure 6.

Static Shape

The same camera combination could be used for 3-dimensional static shape measurements. However, after deployment, the array could be rotated about its axis to different orientations. In particular, measurements were analyzed for the case when the plane of the array is perpendicular to the shuttle's X-axis. These additional results are presented in Table 7. Figure 7 shows two example views for Cameras B and C with the array in this configuration.

For this orientation, acceptable intersection angles can only be obtained when the elbow camera can be used. Thus, the "B-Elbow" pair was used as indicated for deployment results.

Global Dynamic Response

For global dynamic response measurements, the viewing configuration for deployment and static shape measurements is adequate. For dynamic frequency analysis, motion of two of the eight panels is required. So, detailed imagery of a sub-portion of the array is needed to maximize the view of panel oscillation amplitude. With the shuttle cameras zoomed such that a 3 meter wide array panel fills the Horizontal Field of View (HFOV), two 1-meter tall panels fit into the Vertical Field of View (VFOV). Figures 8, 9, and 10 show zoomed views of the top and bottom panels of the array with the array in both parallel and perpendicular orientations.

The angle assessment is the same as presented in Tables 5 and 7. However, in this case, since only one location on the array is being viewed, only unacceptable camera angles to a specific sub-section of the array need to be eliminated from the accuracy analysis. The results of this analysis are shown in Table 8.

These results show that while camera pair "B-Elbow" would provide optimal accuracy over any portion of the array, other camera pairs could provide improved close-up viewing. These camera pairs are summarized in Table 9.

Local Dynamic Response

Finally, the ability to measure detailed dynamic lens motion was considered. In this case, cameras would be zoomed such that the 3-meter wide array would fill the camera's HFOV. Thus, the analysis was identical to the previous assessment for dynamic frequency analysis of sub-panels and recommendations presented in Table 8 apply to this case as well.

Overall, the "B-Elbow" camera combination provided the best combination for acquiring imagery that would support all options. Placing the array on the starboard side of SpaceHab's rooftop improves the viewing accuracy slightly over a port side location. If the Elbow camera is not manifested with the experiment, other camera pairs were shown to have sufficient accuracy to meet structural measurement needs.

For the actual flight experiment, such pre-flight photogrammetric simulations will be used to ensure optimal shuttle camera settings and operations.

Structural Analysis

A critical element of the lightweight solar array concept is the solar concentrator lens that was shown in Figure 2. The highly flexible silicon lens concentrates incident solar energy onto 1 cm wide strips of the highly efficient solar cells which were described in the experiment overview. An optical ray trace diagram illustrating the light concentrating characteristic of this curved Fresnel lens is illustrated in Figure 11.

As seen in the figure, the top-side of the lens is smooth and the bottom-side has a patented Fresnel topography which refracts each incident light ray to a common focal line located slightly above the solar cell strips. For optimal energy collection, the solar energy must maintain a strict pointing requirement. As solar incidence angles become greater than about ± 2.5 degrees, the concentrated solar energy begins to shift away from the solar cell strips, thus, decreasing overall power output of the array.

While the curved Fresnel concept is substantially more tolerant to disturbances than a flat Fresnel lens, structural distortion of the lens or array can still lead to a degradation in optical performance as was shown in a preliminary optical-dynamic analysis of the lens. Such distortion can occur due to thermally induced static shape deformations or due to spacecraft platform disturbances causing dynamic response of the array and lens. These distortions could include local rotation of the lens in amounts that may exceed the pointing requirement or flattening of the lens that leads to an energy loss due to defocusing. Thus, the static and dynamic behavior of the lens during thermal transition periods and disturbance events must be characterized.

In this study, the static and dynamic characteristics of a single lens element were modeled using a continuous representation and a Finite Element Model (FEM) approach. The purpose of the continuous model was investigate the sufficiency of a linear representation to describe the lens behavior and to perform parametric studies. Results from both models were correlated. In later development, the lens FEM will be extended and integrated with the larger array model for a more complete array level structural model.

Lens Description

The geometry of the lens design is shown in Figure 12. The figure shows a schematic of the lens cross-section which is made of a backing layer that is approximately 180 microns thick. A typical prism section is shown in the lower right of Figure 12. The prism geometry varies along the lens cross-section. A representative prism is 100 microns thick and 200 microns wide making the total lens thickness 280 microns. The lens approximates a cylinder section of radius 5.7 cm. Thus, with a width of 9.578 cm, the lens surface spans a 96° arc.

The physical properties of the lens material used in this analysis are given in Table 11. These values are consistent with a test article that was experimentally evaluated during this study. The actual flight test article will use a thinner version of the material currently under development.

Static Analysis of Lens

Continuous Model

A continuous lens model was designed using linear Kirchhoff plate theory¹². Initially, membrane theory was considered because the lenses are thin and highly tensioned. Such a membrane model would predict that the lens will maintain the shape of the support arches along the entire length due to tension in the membrane. However, there is no membrane tension in the lateral direction. So the bending stiffness, however small, dominates structural behavior and allows the lens to flatten out along the longitudinal edges. Membrane theory can not model this stiffness effect. Thus, plate theory was used since it is the simplest theory that correctly predicted the observed lens flattening.

From plate theory, the equations governing the static transverse deflection, w , are

$$D \left(\frac{\partial^4 w}{\partial x^4} + 2 \frac{\partial^4 w}{\partial x^2 \partial y^2} + \frac{\partial^4 w}{\partial y^4} \right) - N_x \frac{\partial^2 w}{\partial x^2} = 0 \quad (1.1)$$

$$w(\pm a/2, y) = \frac{y^2}{2R} \quad (1.2)$$

$$\frac{\partial^2 w}{\partial x^2}(\pm a/2, y) + v \frac{\partial^2 w}{\partial y^2}(\pm a/2, y) = 0 \quad (1.3)$$

$$\frac{\partial^2 w}{\partial y^2}(x, \pm b/2) + v \frac{\partial^2 w}{\partial x^2}(x, \pm b/2) = 0 \quad (1.4)$$

$$\frac{\partial^3 w}{\partial y^3}(x, \pm b/2) + (2 - v) \frac{\partial^3 w}{\partial x^2 \partial y}(x, \pm b/2) = 0 \quad (1.5)$$

where the right hand side of (1.2) is an approximation of the support arch shape, v is Poisson's ratio, and a and b are the lens length and width, respectively. Equations (1.2) and (1.3) represent the simply supported boundary conditions on the supported edges ($\pm a/2$). Equations (1.4) and (1.5) represent the free boundary conditions on the longitudinal edges ($\pm b/2$). The uniform, longitudinal membrane stress in the lens is given by $N_x = E \epsilon_x h_a$, where E is Young's modulus, ϵ_x is the longitudinal strain in the lens, and h_a is the average lens thickness.

Because the lens is corrugated with prisms on one side, care was taken to define the bending stiffness, D , of the lens. To calculate it, a homogenization method is used. In this approach, the effective bending stiffness is determined from the area moment of inertia of a typical lens section as shown in Figure 12. The neutral axis (dashed line) and area moment of inertia, I , of this cross section can be readily determined as $I = \int_A (z - NA)^2 dA = 2.2 \times 10^8 \mu m^4$ and $NA(\text{neutral axis}) = \frac{1}{A} \int_A z dA = -116.5 \mu m$ where z is measured from the top of the lens. The effective bending thickness, h_b , of the lens is then determined from the relation $I = bh_b^3/12$ as $236 \mu m$. The effective prism height is $h_a = A/w_p = 229 \mu m$. The effective bending stiffness can then be determined from

$$D = \frac{E h_b^3}{12(1 - v^2)} \quad (2)$$

To solve the boundary value problem (1) the following transformation is used

$$w(x, y) = \bar{w}(x, y) - \frac{y^2}{2R} + \frac{v}{2R} \left(x^2 - \frac{a^2}{4} \right) \quad (3)$$

Using the non-dimensional terms,

$$\hat{N}_x = N_x a^2 / D \quad \left(\hat{\bar{w}}, \hat{w}, \hat{x}, \hat{y}, \hat{R}, \hat{a}, \hat{b} \right) = (\bar{w}, w, x, y, R, a, b) / a \quad (4)$$

equations (1) become

$$\frac{\partial^4 \hat{\bar{w}}}{\partial \hat{x}^4} + 2 \frac{\partial^4 \hat{\bar{w}}}{\partial \hat{x}^2 \partial \hat{y}^2} + \frac{\partial^4 \hat{\bar{w}}}{\partial \hat{y}^4} - \hat{N}_x \frac{\partial^2 \hat{\bar{w}}}{\partial \hat{x}^2} = \frac{\hat{N}_x v}{\hat{R}} \quad (5.1)$$

$$\hat{\bar{w}}(\pm 1/2, \hat{y}) = 0 \quad (5.2)$$

$$\frac{\partial^2 \hat{\bar{w}}}{\partial \hat{x}^2}(\pm 1/2, \hat{y}) + v \frac{\partial^2 \hat{\bar{w}}}{\partial \hat{y}^2}(\pm 1/2, \hat{y}) = 0 \quad (5.3)$$

$$\frac{\partial^2 \hat{\bar{w}}}{\partial \hat{y}^2}(\hat{x}, \pm \hat{b}/2) + v \frac{\partial^2 \hat{\bar{w}}}{\partial \hat{x}^2}(\hat{x}, \pm \hat{b}/2) = \frac{1 - v^2}{\hat{R}} \quad (5.4)$$

$$\frac{\partial^3 \hat{\bar{w}}}{\partial \hat{y}^3} (\hat{x}, \pm \hat{b}/2) + (2 - \nu) \frac{\partial^3 \hat{\bar{w}}}{\partial \hat{x}^2 \partial \hat{y}} (\hat{x}, \pm \hat{b}/2) = 0 \quad (5.5)$$

The simply supported conditions at $\pm a/2$ are homogenized by this transformation and are satisfied by a solution of the form

$$\hat{\bar{w}}(\hat{x}, \hat{y}) = \sum_m Y_m(\hat{y}) \sin \left[m\pi \left(\hat{x} + \frac{1}{2} \right) \right] \quad (6)$$

The right hand sides of (5.1) and (5.4) can be written as Fourier series

$$\frac{\hat{N}_x \nu}{\hat{R}} = \sum_m G_m \sin \left[m\pi \left(\hat{x} + \frac{1}{2} \right) \right] \quad (7)$$

$$\frac{1 - \nu^2}{\hat{R}} = \sum_m H_m \sin \left[m\pi \left(\hat{x} + \frac{1}{2} \right) \right]$$

so that dependence on the longitudinal coordinate, x , is removed when (6) is used in (5). The result is an ordinary differential equation for Y_m ,

$$\frac{\partial^4 Y_m}{\partial \hat{y}^4} - 2m^2 \pi^2 \frac{\partial^2 Y_m}{\partial \hat{y}^2} + (m^4 \pi^4 - m^2 \pi^2 \hat{N}_x) Y_m = G_m \quad (8)$$

with boundary conditions

$$\frac{\partial^2 Y_m}{\partial \hat{y}^2} (\pm \hat{b}/2) - \nu m^2 \pi^2 Y_m (\pm \hat{b}/2) = H_m \quad (9)$$

$$\frac{\partial^3 Y_m}{\partial \hat{y}^3} (\pm \hat{b}/2) - (2 - \nu) m^2 \pi^2 \frac{\partial Y_m}{\partial \hat{y}} (\pm \hat{b}/2) = 0$$

that can be readily solved. The transverse deflection is then determined from the solution for Y_m using (6) and (3) and is given as

$$Y_m = \frac{G_m}{m^4 \pi^4 - m^2 \pi^2 \hat{N}_x} + A_m \cosh(\lambda_1 \hat{y}) + B_m \cosh(\lambda_2 \hat{y}) \quad (10.1)$$

where

$$\lambda_1^2 = m\pi \left(m\pi - i\sqrt{\hat{N}_x} \right)$$

$$\lambda_2^2 = m\pi \left(m\pi + i\sqrt{\hat{N}_x} \right)$$

A_m and B_m are found from the boundary conditions as

$$A_m = \frac{\lambda_2 [\lambda_2^2 + (2 - \nu) m^2 \pi^2] [G_m \nu + H_m (m^2 \pi^2 + \hat{N}_x)] \sinh(\hat{b} \lambda_2 / 2)}{P_m} \quad (10.2)$$

$$B_m = \frac{-\lambda_1 [\lambda_1^2 + (2 - \nu) m^2 \pi^2] [G_m \nu + H_m (m^2 \pi^2 + \hat{N}_x)] \sinh(\hat{b} \lambda_1 / 2)}{P_m} \quad (10.3)$$

where

$$P_m = (m^2 \pi^2 + \hat{N}_x) \left\{ \lambda_1 [\lambda_1^2 + (2 - \nu) m^2 \pi^2] [m^2 \pi^2 \nu - \lambda_2^2] \cosh(\hat{b} \lambda_2 / 2) \sinh(\hat{b} \lambda_1 / 2) \right. \\ \left. - \lambda_2 [\lambda_2^2 + (2 - \nu) m^2 \pi^2] [m^2 \pi^2 \nu - \lambda_1^2] \cosh(\hat{b} \lambda_1 / 2) \sinh(\hat{b} \lambda_2 / 2) \right\} \quad (10.4)$$

$$G_m = \frac{2\hat{N}_x v [1 - (-1)^m]}{m\pi\hat{R}} \quad (10.5)$$

and

$$H_m = \frac{2(1 - v^2) [1 - (-1)^m]}{m\pi\hat{R}} \quad (10.6)$$

The complete solution is

$$\hat{w}(\hat{x}, \hat{y}) = \sum_m Y_m \sin \left[m\pi \left(\hat{x} + \frac{1}{2} \right) \right] - \frac{\hat{y}^2}{2\hat{R}} + \frac{v}{2\hat{R}} \left(\hat{x}^2 - \frac{1}{4} \right) \quad (11)$$

Finite Element Model (FEM)

A discrete representation of the lens was made using plate elements in NASTRAN¹³. The end boundary conditions were pinned to prevent translations but allow rotations. The longitudinal edges were free to rotate and translate. A tension load of 1.12 N was applied to each end to produce a 4% strain in the lens.

Static Response

Static results from both models were correlated using design parameters from Table 11. The continuous model was then used to generate the parametric trends discussed below.

The results showed that significant edge flaring or flattening of the lens occurred away from the end supports. The distortion from the arch shape is greatest at the lens mid-span as illustrated in Figure 13. Increasing the strain in the lens reduces the flattening. Figure 14 shows the amount of distortion away from the nominal arched shape at the lens mid-span from the mid-width to the free edge. The deformation is symmetric with respect to the mid-width. As seen in the figure, the distortion is greatest at the free edges of the lens. For the nominal 2% lens strain, the maximum free-edge distortion is 3.6 mm. Increasing the lens strain to 10% (a value much too large for the application) reduces the free-edge distortion to 1.6 mm. At the practical limit of 4%, the free-edge distortion is 2.5 mm.

The lens flattening can also be reduced by making the lens thinner, thus, reducing the bending stiffness. While the thickness of the prisms is specified by the optical design, the backing layer can be made thinner. 3M is currently working to reduce the backing layer thickness from 180 to 90 μm . This will help alleviate flattening. For 4% lens strain, Figure 15 shows how the mid-span distortion changes with backing thickness. A reduction in backing thickness from 180 to 90 μm reduces the free-edge distortion from 2.5 to 1.6 mm.

Figure 16 shows the free-edge distortion as a function of the lens length. As length increases, the free-edge distortion also increases. Since the overall length of the lens is fixed by the solar panel geometry, so, a recommendation was made to use shims with the correct arch shape to reduce the effective length. These shims would be much stiffer than the lens but flexible enough to be stowed flat and can be installed along the lens length. This result had a critical impact on the lens design as it directly effects the overall power performance of the solar array.

Finally, it is noted that as the deformation imposed at the ends by the supports becomes large compared to the lens thickness, a non-linear plate theory should be used. For the current study, however, linear plate theory was shown to be adequate to predict the observed static shape behavior of the tensioned lens. Further non-linear analysis using the continuous model will be performed in a follow-on study.

Dynamic Analysis of Lens

Continuous Model

Linear cylindrical shell theory was used to predict the natural frequencies and mode shapes of the lens. The free response of the lens was determined using linear shell theory. In this theory, the in-plane and transverse

motion of the lens was coupled. The lens was assumed to have been deformed into a circular cylindrical section as shown in Figure 11. The equations of equilibrium for transverse (w), lateral (v), and longitudinal (u) motion were coupled and too lengthy to reproduce here¹⁴. The lens was tensioned with a uniform longitudinal stress. The unsupported edges were assumed to be moment and traction free. The transverse and lateral displacements at the support edges were set to zero. No moment acted on these edges and the lens was free to contract in the longitudinal direction.

With these boundary conditions, solutions of the form

$$u(x, y, t) = U(y) \cos[n\pi(x/L + 1/2)] \exp[i\omega t] \quad (12.1)$$

$$v(x, y, t) = V(y) \sin[n\pi(x/L + 1/2)] \exp[i\omega t] \quad (12.2)$$

$$w(x, y, t) = W(y) \sin[n\pi(x/L + 1/2)] \exp[i\omega t] \quad (12.3)$$

satisfy the supported end conditions and remove dependence on x and t from the equations of motion. The resulting ordinary differential equations can be readily solved to find the free response of the lens. The differential equations of motion are given as

$$\frac{1-v}{2} \frac{\partial^2 u}{\partial^2 y} + \frac{v}{R} \frac{\partial w}{\partial x} + \frac{1+v}{2} \frac{\partial^2 v}{\partial x \partial y} + \left(1 + \frac{N_x}{K}\right) \frac{\partial^2 u}{\partial^2 x} = \frac{\rho}{K} \frac{\partial^2 u}{\partial^2 t} \quad (13.1)$$

$$\frac{\partial^2 v}{\partial^2 y} + \frac{1}{R} \frac{\partial w}{\partial y} + \frac{1+v}{2} \frac{\partial^2 u}{\partial x \partial y} u_{xy} + \left(\frac{1-v}{2} + \frac{N_x}{K}\right) \frac{\partial^2 v}{\partial^2 x} = \frac{\rho}{K} \frac{\partial^2 v}{\partial^2 t} \quad (13.2)$$

$$-\frac{D}{K} \left(\frac{\partial^4 w}{\partial^4 x} + 2 \frac{\partial^4 w}{\partial^2 x \partial^2 y} + \frac{\partial^4 w}{\partial^4 y} \right) - \frac{1}{R} \left(\frac{\partial v}{\partial y} + v \frac{\partial u}{\partial x} \right) + \frac{N_x}{K} \frac{\partial^2 w}{\partial^2 x} - \frac{w}{R^2} = \frac{\rho}{K} \frac{\partial^2 w}{\partial^2 t} \quad (13.3)$$

Dynamic Response

The continuous and finite element models were used to predict natural frequencies and mode shapes of the lens. Results were correlated and the continuous model was used to perform a parametric study. The parametric study focused on how lens strain and thickness alter lens natural frequencies.

Using the nominal parameter values given in Table 11, a mass density of 1080 kg/m³ and both h_a and h_b as 150 μ m, the natural frequencies and mode shapes of the lens were calculated. The first six longitudinal ($n = 1$) modes are shown in Figure 17 as the cross-width deformation at the lens mid-span and with the corresponding natural frequencies. The dotted line represents the reference, circular shape of the lens cross section. The solid black and gray lines show the shapes of the cross section at the peak displacement. The lowest mode is the first torsion mode in which the lens is rotating about the mid-width ($y = 0$) axis. The second mode is a bending mode that is very accurately predicted by beam theory for this slender shell. The fourth mode is a sway mode in which the lens is predominantly moving laterally.

It was shown previously that increasing the strain in the lens decreases the static lens shape distortion. The strain also affects the natural frequencies as shown in Figure 18. As anticipated, the natural frequencies increase with increasing lens strain. The first longitudinal modes ($n = 1$) increase at the lowest rate with increasing strain. The lowest natural frequency for each longitudinal mode number (n) is accurately forecast by Euler-Bernoulli beam theory with pinned ends which predicts natural frequencies (in Hz) at

$$F_n = \frac{1}{2\pi} \sqrt{\frac{EI_{zz}n^4\pi^4}{L^4\rho A} + \frac{E\epsilon_x n^2\pi^2}{L^2\rho}} \quad (14)$$

where I_{zz} is the area moment of inertia of the arched cross section (465 mm), and A is the cross sectional area (14.4 mm).

As the thickness of the lens can be varied without affecting the optical performance, it is important to understand how the natural frequencies change with thickness. In this flexible, highly tensioned lens, it is not expected that the lowest natural frequencies for a given n would vary greatly with thickness. This is demonstrated by studying which showed that the lowest natural frequency for a given n is accurately predicted by this equation. For the current case, the second term in (14), which does not change with thickness, is much greater than the first. Thus, for all practical lens thicknesses the second term dominates the first and determines the lowest natural frequency for each n. The full shell analysis confirms this simple beam analysis. As seen in Figure 19 (with $\epsilon_x = 4\%$), the lowest natural frequencies for n=1 and n=2 are nearly constant for lens thicknesses ranging from 50 to 200 μm . For each n, the higher modes increase with increasing thickness as expected. Points showing frequencies from the finite element model for the first three modes are also shown in this figure indicating correlation of the two models. Figure 20 illustrates these modes.

Also as seen in Figure 19, as the thickness decreases to zero, all the modes with the same n collapse to the natural frequencies (in Hz) predicted by string theory.

$$F_n = \frac{n}{2L} \sqrt{\frac{E\epsilon_x}{\rho}} \quad (15)$$

The first and second sway modes also do not change greatly in this range of lens thicknesses. These modes are also accurately predicted by beam theory (a) with the appropriate area moment of inertia, I_{zz} .

Structural Dynamics of Array

AEC-Able provided LaRC with a NASTRAN model of the flight test article for dynamic analysis. The model included the 8 composite panels, representation of panel connections and support hardware. This model did not include definition of the individual lens elements. Figures 21 a) through c) show the first three modeshapes of the array. It is seen that the first mode is the first bending mode at 0.1 Hz. In at least the next 10 modes, vibration is dominated by mode localization and modal frequencies are very closely spaced (Table 12). This is due to the array's 'picture frame' design wherein the center of the panel has been thinned to reduce mass.

Dynamic Load Response of Array

As part of the dynamic analysis, an attempt was made to characterize the shuttle disturbance environment and to determine the level of response of the array to base motion.

The disturbance characterization involved taking a qualitative look at the typical response levels associated with Shuttle Reaction Control System (RSC) jet firings^{15,16,17,18}. Since there is no frequency transfer function data known to be available between thrusters and the SpaceHab rooftop, data from other microgravity experiments was considered in order to get a order-of-magnitude estimate of response levels from other SpaceHab locations.

In particular, representative data from the Space Acceleration Measurement System (SAMS) experiments on STS-57, STS-79 and STS-89 was considered. The purpose of this series of experiments was to characterize the microgravity environment on SpaceHab due to routine shuttle events such as reaction control jet firings and MIR docking operations.

The primary source considered in the current experiment for dynamic excitation was the reaction control system jet firings. Thus, SAMS data showing acceleration responses to such excitation were reviewed. Table 13 summarizes the overall capability of the primary (PRCS) and vernier (VRCS) reaction control system and the range of acceleration responses observed. Figures 22 and 23 show typical responses of PRCS and VRCS on the Spacehab Module. The use of PRCS would likely cause the 0.015g design load limit on the array to be

exceeded. However, the VRCS can be controlled to produce excitation without exceeding the design load limit. Additional disturbance characterization work is required in the Formulation Phase to more exactly define thruster firing sequences and geometries that would be used to excite the array in this experiment. Such analysis would necessarily include more specific structural details about the SpaceHab module and the Space Shuttle's mass configuration for the proposed flight.

Since the actual disturbance environment required additional refinement, some initial dynamic responses of the array to assumed base-motions were computed. All disturbances were input at the base and normal to the array plane. Five percent (5%) damping was assumed in the array. The purpose was to determine what level of input was required to produce a reasonable displacement for photogrammetric measurements. Two cases were considered.

First, the array was subjected to a series of pulses with amplitudes of 0.015, 0.15 and 1.5 g's, each applied for durations of 0.01, 0.1, 1 and 2 seconds. The maximum displacement observed in each case is shown in Figure 24. 0.015g is the maximum normal acceleration allowable according to upper level design requirements. For this case, a peak response of 0.065 inches was observed due to a pulse duration of 2 seconds. This would be barely adequate for photogrammetric measurements which can resolve a minimum of 0.06 inches at the tip as was shown in Table 9.

Second, the array was subjected to a series of pulses designed to excite the array's first bending frequency at 0.1 Hz and to more closely model a thruster firing. The pulses were 10 seconds in duration and included a 3 second pulse duration and a 7 second pause. A series of 1, 2 or 3 sets of pulses were input and the amplitude required to produce 3, 5, and 10 inches of tip motion was noted. Results of this analysis are shown in Figure 25.

The results of these base-motion simulations showed that it is likely that thruster firings can be designed to produce an adequate level of tip motion for photogrammetric measurement and analysis. However, the maximum normal acceleration specified in upper level design requirements may need to be increased by a factor of 10 (ie. increase to 0.15g) in order to achieve this.

Experimental Ground Tests

1 meter SLA Structural Dynamics

A representative 1-meter stretched lens element under 2% strain was provided to LaRC by NMP partner ENTECH for experimental evaluation. The test set-up is shown in Figure 26. For the evaluation, 40 circular targets were attached to the lens at regular intervals and a shaker was attached to the membrane support structure to introduce disturbances normal to the plane of the lens. Using a scanning laser vibrometer in the laboratory environment, the first two modes of the lens were obtained. The first mode observed was a 2.3 Hz bending mode and the second was a 2.9 Hz torsion mode.

These frequencies are slightly lower than predicted by the lens analysis as shown in Figure 19 by the triangles. Also, the order of first bending and first torsion modes is reversed. Several uncertainties exist which could explain such differences. First, uncertainty in the lens boundary conditions, effective thickness and tension may cause such variation. The natural frequency of the lens was shown by analysis to be a strong function of the tension. Second, the total lens thickness is only 300 microns. Thus, dynamic results could vary from predicted values due to aeroelastic mass and damping effects of the surrounding air. Such change in dynamic performance of a vibrating membrane as a function of air pressure was shown in a previous NASA publication¹⁹.

Mini-camera Simulation

In order to more fully characterize local dynamic motion of the lens elements, it was proposed to use wireless mini-cameras mounted under individual lens elements. Space Shuttle video camera would provide cost-effective photogrammetric measurements of the overall structure with good accuracy but would provide only fair to poor measurement accuracy for individual lenses because of the distances and geometry involved.

Thus, for this concept, up to about 4 inactive lens elements (ie. not instrumented with photovoltaic cells) would be used. The lenses would be covered with approved targets and/or patterns to permit visualization. Lens surface treatments would be used to vary the optical transmissivity of the lens and reduce background light and reflection.

Figure 26 shows how these cameras might look mounted behind the 1-meter stretched lens. The cameras shown are board-level cameras and suitable for the space environment. The laboratory example shows the how the cameras are oriented at oblique angles under a lens. These oblique views are required for 3D photogrammetric triangulation. Typical views from these cameras are shown in Figure 27.

Measurement System Concept Definition

A measurement system concept that meets the structural measurement objectives was defined and is presented in this section. The concept design was based on the preliminary analytical and experimental evaluation of the solar array test article and was constrained by resource and cost limitations. In particular, it was desirable to achieve the structural measurement objectives using a system with the lowest possible mass without introducing risk into other elements of the flight demonstration.

In general, it was decided that the global and local structural behavior of the solar array will be determined using photogrammetry with images from the Space Shuttle's standard camera system, array based accelerometers and mini-cameras mounted under a limited number of array lens elements. Structural data will be obtained during the following prescheduled, structural excitation events:

1. Camera calibration
2. Array deployment
3. Array rotation
4. Daylight with scheduled VRCS pulsed firings
5. Day/night transitions with scheduled VRCS pulsed firings
6. Nighttime with artificial illumination
7. Array solar tracking
8. Array retraction.

The following is a description of data acquisition from sensors and the operations concept. A diagram of the system architecture is shown in Figure 28. It is estimated that the added mass of this system will be 20 kg or less if state-of-the art data acquisition and storage systems are used. The system will be refined during further development in the Formulation Phase.

Standard Shuttle Camera System

For this experiment, at least two Space Shuttle Color Television Cameras (CTVC) will be used for monitoring the global, structural dynamic behavior of the solar array. If the Remote Manipulator Arm (RMA) is manifested, the RMA Elbow camera will be utilized. In addition, two of the fore- and aft- bulkhead payload bay mounted cameras will be used. It is assumed, for example, that if the RMA is manifested on the port side, then port side cameras and the elbow camera would be used. In this configuration, the solar array should be mounted on the starboard side of SpaceHab's Research Module rooftop for maximum photogrammetric accuracy as already determined by JSC's Image Analysis Lab.

The Shuttle's Close Circuit Television System (CCTV) will record time synchronized on-orbit video signals in digital NTSC format on mini-DVCAM digital cassettes during the prescheduled excitation events. An additional channel will be down-linked to JSC via standard shuttle communication links for periodic monitoring of SLA events if a Tracking and Data Relay (TDRS) satellite is in line-of-sight (LOS) view of the Shuttle.

Shuttle cameras settings and orientations will be controlled from the ground via standard Shuttle operating procedures. A majority of these settings will be uplinked during crew sleep hours. Array events should be scheduled such that LOS view is available during array events for the purpose of periodic monitoring of array dynamic behavior. Camera data recording will be synchronized with pre-scheduled array events to begin at least

30 seconds before and end approximately 3 minutes after such events. If timeline changes occur, recording control may be changed via ground communication. Astronauts will be required to change digital cassette tapes at scheduled times during operations.

Pre-flight and in-flight calibration of the cameras will be performed in order to optimize photogrammetric accuracy. Photogrammetric accuracy in the experiment will be calculated based on known coordinates and/or separation distances of several stationary control points in the images.

Array-Based Measurement System

The array-based measurement system includes the mini-cameras and accelerometers. Power connections for all these devices would be provided on a common array source by AEC-Able. The power at this source originates from SpaceHab and crosses the solar array slip-ring to provide power to array based instrumentation.

In-Situ Accelerometers

Six (6) accelerometers will be used as shown in Figure 29. Three Honeywell QA-1400 accelerometers will be mounted at array tip locations to measure in-plane and out-of-plane acceleration. The other three will be located at the solar array base to measure 3-axis translation excitation to the array. The SpaceHab-provided data acquisition system for AEC-Able would be responsible for controlling and storing the data from these sensors.

Mini-Cameras

Up to eight (8) mini-cameras will be located at several locations under the SLA lenses for the purpose of monitoring the stretched lens' dynamic response. To facilitate viewing of lens motion, patterns or targets will be placed on in-active lens elements.

Signals from these devices will be sent to an antenna via wireless transmission at a JSC-approved frequency. Sensor signals will be spaced at 10MHz intervals within this band to prevent interference. The receiving antenna and signal amplifier will be externally mounted on the SpaceHab rooftop within line-of-sight (LOS) of the transmitters. LaRC would provide the space qualified mini-cameras, antenna, and signal amplifier. SpaceHab will provide a standard power source for the antenna and signal amplifier.

SpaceHab will provide two low-loss coax cable connections between the externally mounted amplifier and the NASA LaRC provided Data Acquisition Equipment (LDAQ) inside SpaceHab. The LDAQ will include multiple signal receivers, high-volume data storage device, a laptop for control and video monitoring, a camera selector switch, power and network interfaces. SpaceHab will provide a non-interrupted standard power supply. LDAQ equipment will be space qualified by LaRC or its contractors. The laptop will interface with a standard high-rate 100BaseT ethernet line for periodic down-link of compressed images and up-link of control commands. A standard IRIG-B time signal, correlated with Shuttle mission time, will be provided by SpaceHab to the LDAQ.

Control of the mini-cameras will be pre-programmed into the laptop. Changes may be made via ground communication without astronaut interaction. Data recording will be synchronized with pre-scheduled array excitation events to begin at least 30 seconds before and end approximately 3 minutes after such events. If timeline changes occur, control commands in the laptop may be rescheduled via the 'SpaceHab to ground' communication link.

Pre-defined sections of data from mini-cameras will be periodically digitized and compressed as needed for downlink to the payload operations center (POC). The volume and frequency of transmission will be tailored to fit the constraints of the standard SpaceHab data communication system. Such downlink will be limited to calibration and appropriate periodic sampling for the purpose of system performance monitoring.

Accelerometer data will be acquired continuously throughout array excitation events, deployment and retraction. With input from LaRC, predefined sections of data will be downlinked to the POC from the AEC-Able data system for safety and performance monitoring.

Astronauts will be required to change data storage media of the LDAQ at scheduled times during operations. Astronauts will also be required to periodically monitor video channels on the LDAQ via the laptop computer to verify correct operation of the system.

Shuttle Spacecraft Operations

The Space Shuttle will be required to perform preplanned VRCS jet firings in order to provide dynamic structural excitation of the array. These firings will be designed to be consistent with shuttle operational requirements. Astronauts may be required to rotate the array or perform orbiter attitude change for optimal photogrammetric lighting conditions.

Ground Support Architecture - Payload Operations Center (POC)

The NASA LaRC team will collocate with AEC-Able at the designated Payload Operations Center (POC) during the mission. LaRC will provide a data analysis computer and supporting peripheral equipment. LaRC will also provide a computer interface to the electronic communications link for ground control and monitoring of the array-based measurement system electronics. This interface and its operation will conform to SpaceHab protocol.

Data Processing

Limited data which is down-linked to the NASA LaRC Team during the mission will be analyzed at the POC. The purpose of this analysis will be to assess adequate lighting conditions and dynamic response amplitudes for the photogrammetric measurements and to derive an initial estimate of structural behavior. Full data analysis of the Shuttle camera, mini-camera and accelerometer data will begin upon receipt of the data storage media following the flight experiment.

Shuttle camera images will be analyzed by NASA LaRC investigators in collaboration with the NASA JSC Image and Analysis Group. In this analysis, 3D coordinates as a function of time will be computed for various targets and distinguishable features in the images that appear in two or more camera views. To achieve this, image registration will be conducted using known coordinates and/or separation distances of several stationary points to calculate pointing angles and other properties of the cameras. Target tracking will be performed to create X and Y image-plane time histories of each target. Targets in each image will be referenced with the corresponding target in other images. Finally, two or more sets of X and Y image-plane data sets and camera parameters will be triangulated to obtain the 3D motion time histories. Photogrammetric accuracies will also be calculated and assessed.

The 3D motion time histories, mini-camera images and accelerometer data will be evaluated at NASA LaRC. Deployment dynamics and static shape will be compared to analytical predictions at each measurement point. To obtain structural modal parameters, transient free-decay dynamic responses will be analyzed using a time-domain procedure such as the Eigensystem Realization Algorithm (ERA)²⁰. ERA calculates modal parameters (natural frequencies, damping factors, and mode shapes) from the transient time histories. Analytical models will then be validated against results.

All data and results will be stored and available upon request in a variety of formats.

Summary

In summary, a measurement system was designed for structural characterization of a lightweight solar array deployed from the Space Shuttle cargo bay. As part of the concept design study, measurement system objectives were defined and initial analysis and experimental evaluation of the solar array were performed. The analysis showed that the array demonstrated low-frequency dynamic behavior with mode localization due to the panel cut-out design. The lenses showed closely spaced modal behavior with frequencies being a strong function of membrane tension. Static analysis led to a critical improvement in lens design. Early dynamic response analysis

showed that the Shuttle's VRCS will provide sufficient excitation to the array for structural characterization measurements. Experimental evaluation of a lens element showed that photogrammetric measurements of the lens motion are feasible, although challenges remain in dealing with variable lighting conditions. In addition, currently available photogrammetric measurement systems were traded to determine the optimal system for the proposed shuttle-based experiment. The standard Shuttle camera system was selected for use along with mini-cameras mounted under solar concentrator lenses and solar array based accelerometers. A preliminary system design and operations concept was defined.

References

1. Brumfield, M.L., Pappa, R.S., Miller, J.B., and Adams, R.R., "Orbital Dynamics of the OAST-1 Solar Array Using Video Measurements," AIAA Paper No. 85-0758-CP, presented at AIAA/ASME/ASCE/AHS 26th Structures, Structural Dynamics and Materials Conference, Orlando, FL, April 15-17, 1985.
2. Gilbert, M.G., Welch, S.S., Pappa, R.S., Demeo, M.E., "STS-74/MIR Photogrammetric Appendage Structural Dynamics Experiment Preliminary Data Analysis", AIAA Paper 97-1168, 38th AIAA Structures, Structural Dynamics and Materials Conference, Kissimmee, FL, Apr. 7-10, 1997.
3. Glo Experiment/Photogrammetric Appendage Structural Dynamics Experiment Payload (Hitchiker), "Payload Integration Plan (PIP) Basic," NASA Johnson Space Center Document NSTS 21316, Feb. 1995.
4. SpaceHab Documentation, MDC 91W5023K, pp 4-2 to 4-3, June, 2000.
5. M.J. O'Neill, "Solar Concentrator and Energy Collection System," U.S. Patent 4,069,812, 1978
6. M.J. O'Neill, "Color-Mixing Lens for Solar Concentrator System and Methods of Manufacture and Operation Thereof," U.S. Patent 6,031,179, 2000.
7. M.J. O'Neill, "Stretched Fresnel Lens Solar Concentrator for Space Power," U.S. Patent 6,075,200, 2000.
8. Informal communication with Mark O'Neill at ENTECH, Inc.
9. "New Millennium Program Space Technology 6 (ST-6) Technology Announcement," NASA JPL, Oct. 10, 2000.
10. NASA JSC Image Science and Analysis Group, "Mensuration Support Proposal for the Lightweight High-Voltage Stretched-Lens Concentrator Solar Array Experiment," July, 2001.
11. *Pro/ENGINEER*, PTC, Needham, MA.
12. S. Timoshenko and S. Woinowsky-Krieger, *Theory of Plates and Shells*, New York, McGraw-Hill, 1959.
13. *MSC NASTRAN*, MSC Software Corporation, Santa Anna, CA.
14. W. Soedel, *Vibrations of Shells and Plates*, New York, Marcel Dekker, 1993.
15. "Microgravity Environment Description Handbook," NASA TM-107486, 1997.
16. Finley, B., Grodsinsky, C., and DeLombard, R., "Summary Report of Mission Acceleration Measurements for SPACEHAB-01, STS-57," NASA TM 106514, March 1994.
17. Rogers, M. J. et al, "Summary Report of Mission Acceleration Measurements for STS-79," NASA CR 202325, 1996.
18. Hrovat, K. and McPherson, K., "Summary Report of Mission Acceleration Measurements for STS-89," NASA TM 209084, 1999.
19. Sewall, J.L, Miserentino, R., and Pappa, R. S., "Vibration Studies of a Lightweight Three-Sided Membrane Suitable for Space Application," NASA TP-2095, Jan. 1983.
20. Juang, J.-N. and Pappa, R. S., "An Eigensystem Realization Algorithm for Modal Parameter Identification and Model Reduction," *Journal of Guidance, Control, and Dynamics*, Vol. 8, No. 5, September-October 1985, pp. 620-627.

Table 1 NMP ST-6 Performance Specifications

Power Generation Capability of Deployed Array*	~7kW
Power Density*	>175 W/kg
Output Voltage*	≥ 300 V
Capability of Operating at Distances from the Sun	1 to 5 AU
Test Article Power Generation at 1 AU	>500W
Stowed Volume	< 1.5m ³
* At 1 Astronomical Unit (AU) from the Sun when fully populated with solar cells.	

Table 2 Relevant Array Specifications

Solar Array Mass	50 kg
Deployed Height	9 meters
Deployed Width	3 meters
First Bending Frequency	0.1 Hz
First Torsion Frequency	1 Hz
Normal Load Limit	0.015g
Deployment Time	2- 5 minutes

Table 3 Measurement System Hardware Specifications

INSTRUMENT	Flight Qualification Status	SENSOR						LENS		
		Calibration	Pixel	Mono	Grayscale	TYPE	Digital/ Analog	Field of View (FOV)	Frame Rate	Fixed/ Zoom
Standard Shuttle Payload Bay Cameras	Yes	PRE	648X480	Color	8 BIT	Interlaced	Analog	10-70 deg.	30	Zoom
Laser Dynamic Range Imager (LDRI)	Yes	POST	640x480	Yes	8-12 BIT	Progressive	Analog	40 deg.	30/7.5	Fixed
LCS	Yes	PRE/POST	1024x1024	Yes	13 BIT	Progressive	Digital	30 deg.	30	Zoom
PASDE Lite	No	PRE/POST	648x480	Yes	8 BIT	Interlaced	Analog	15 deg.	30	Fixed



Table 4 Measurement System Operational Specifications

INSTRUMENT	Power	Added Payload Weight	Lighting Conditions			Tracking	Operational Wavelength	Range	Processing		DownLink
			Sun	Shade	Night				Real-Time	Post	
Standard Shuttle Payload Bay Cameras	N/A	N/A	Yes	Yes	No*	Yes	380>	200'	Yes	Yes	Yes
Laser Dynamic Range Imager (LDRI)	28VDC	6 lbs.	No	No	Yes	No	850nm	150'	Yes	Yes	Yes
LCS	28VDC	25 lbs.	Yes	Yes	Yes	Yes	805nm	100'	No	Yes	Yes
PASDE Lite	**	**	Yes	Yes	No	No	380>	**	No	Yes	No

* Possible with artificial illumination

Table 5
Intersection Angle (degrees) to a Point on the Axis of Rotation:
Array Plane Parallel to Orbiter X-Axis

For close-range photogrammetry:

-  Intersection angles <30° or >150° are unstable
 Intersection angles <45° or >140° are undesirable

For the Array Located on the Port Side of the SpaceHab

Camera Pair	Base of the Array	Middle of the Array	Top of the Array
A - B	158.2	111.5	80.1
B - Elbow	131.6	73.3	45.7
C - D	138.8	106.6	78.4

For the Array Located on the Starboard Side of the SpaceHab

Camera Pair	Base of the Array	Middle of the Array	Top of the Array
A - B	138.8	106.6	78.4
B - Elbow	100.9	67.6	44.3
C - D	158.2	111.5	80.1

Table 6
Axial Dimensions (inches) of Uncertainty Volume to a Point on the Axis of Rotation:
Array Plane Parallel to Orbiter X-Axis

For the Array Located on the Port Side of the SpaceHab

Camera Pair	Base of the Array	Middle of the Array	Top of the Array
B - Elbow	0.25, 0.1, 0.1	0.26, 0.19, 0.19	0.51, 0.32, 0.32
C - D	0.58, 0.21, 0.21	0.43, 0.27, 0.27	0.5, 0.37, 0.37

For the Array Located on the Starboard Side of the SpaceHab

Camera Pair	Base of the Array	Middle of the Array	Top of the Array
A - B	0.58, 0.21, 0.21	0.43, 0.27, 0.27	0.5, 0.37, 0.37
B - Elbow	0.21, 0.14, 0.14	0.29, 0.21, 0.21	0.51, 0.33, 0.33

Table 7
Intersection Angle (degrees) to a Point on the Axis of Rotation:
Array Plane Perpendicular to Orbiter X-Axis

For the Array Located on the Port Side of the SpaceHab

Camera Pair	Base of the Array	Middle of the Array	Top of the Array
A - D	17.1	15.6	13.2
B - C	40.1	30.5	21.4
D - Elbow	44.4	46.2	39.1

For the Array Located on the Starboard Side of the SpaceHab

Camera Pair	Base of the Array	Middle of the Array	Top of the Array
A - D	17.1	15.6	13.2
B - C	40.1	30.5	21.4
D - Elbow	55.3	49.8	39.1

Table 8
Axial Dimensions (inches) of Uncertainty Volume to a Point on the Axis of Rotation:
Array Plane Perpendicular to Orbiter X-Axis

For the Array Located on the Port Side of the SpaceHab

Camera Pair	Base of the Array	Middle of the Array	Top of the Array
D - Elbow	0.54, 0.1, 0.1	0.58, 0.19, 0.19	0.78, 0.32, 0.32

For the Array Located on the Starboard Side of the SpaceHab

Camera Pair	Base of the Array	Middle of the Array	Top of the Array
D - Elbow	0.45, 0.14, 0.14	0.54, 0.21, 0.21	0.75, 0.33, 0.33

Table 9
Axial Dimensions (inches) of Uncertainty Volume to a Point on the Axis of Rotation:
Array Plane Perpendicular to Orbiter X-Axis and Zoomed Cameras

Plane of Array Parallel to X-Axis of Orbiter

For the Array Located on the Port Side of the SpaceHab

Camera Pair	Base of the Array	Middle of the Array	Top of the Array
A - B		0.11, 0.06, 0.06	0.09, 0.07, 0.07
B - Elbow	0.16, 0.06, 0.06	0.09, 0.06, 0.06	0.11, 0.07, 0.07
C - D	0.18, 0.07, 0.07	0.11, 0.07, 0.07	0.09, 0.07, 0.07

For the Array Located on the Starboard Side of the SpaceHab

Camera Pair	Base of the Array	Middle of the Array	Top of the Array
A - B	0.2, 0.07, 0.07	0.11, 0.07, 0.07	0.09, 0.07, 0.07
B - Elbow	0.13, 0.09, 0.09	0.1, 0.07, 0.07	0.11, 0.07, 0.07
C - D		0.11, 0.06, 0.06	0.09, 0.06, 0.06

Plane of Array Perpendicular to X-Axis of Orbiter

For the Array Located on the Port Side of the SpaceHab

Camera Pair	Base of the Array	Middle of the Array	Top of the Array
B - C	0.11, 0.06, 0.06	0.13, 0.06, 0.06	
D - Elbow	0.34, 0.06, 0.06	0.2, 0.06, 0.06	0.16, 0.07, 0.07

For the Array Located on the Starboard Side of the SpaceHab

Camera Pair	Base of the Array	Middle of the Array	Top of the Array
B - C	0.11, 0.06, 0.06	0.13, 0.06, 0.06	
D - Elbow	0.22, 0.07, 0.07	0.17, 0.07, 0.07	0.15, 0.07, 0.07

Table 10 Acceptable camera pairs for dynamic analysis

Array Panels Viewed

Array Location on SpaceHab Rooftop	Bottom	Middle	Top
Port Side	B - C with array perpendicular to X-Axis	B - Elbow with array parallel to X-Axis	A - B or C - D with array parallel to X-Axis
Starboard Side	B - C with array perpendicular to X-Axis	B - Elbow with array parallel to X-Axis	A - B or C - D with array parallel to X-Axis

Table 11 Parameter Values for Structural Analysis

Parameter	Nominal Value	Units
a	1	m
b	9.578	cm
E	1.758	MPa
h_a	229	mm
h_b	236	mm
R	5.7	cm
μ_k	0.02	-
ρ	1080	Kg/m ³
ν	0.45	-

Table 12 First 10 Modal Frequencies of Array

Mode	Natural Frequency (Hz)
1	0.1
2	0.377
3	0.383
4	0.415
5	0.419
6	0.421
7	0.421
8	0.446
9	0.448
10	0.449

Table 13 Shuttle Reaction Control System (RSC) Input Forces and Typical Reponse Levels

Thruster	Number of Thrusters	Force	Duration	Peak Acceleration Response
Primary Reaction Control System (PRCS)	38	870 lbs	Pulse Mode: 0.08 msec min Steady-State Mode: 1-150 sec	6 - 55 mg's
Vernier Reaction Control System (VRCS)	6	24 lbs	Pulse Mode: 0.08 msec min Steady-State Mode: 1-125 sec	0.3 - 0.7 mg's

* PRCS excites orbiter modes at 3.5, 4.7, 5.1 Hz

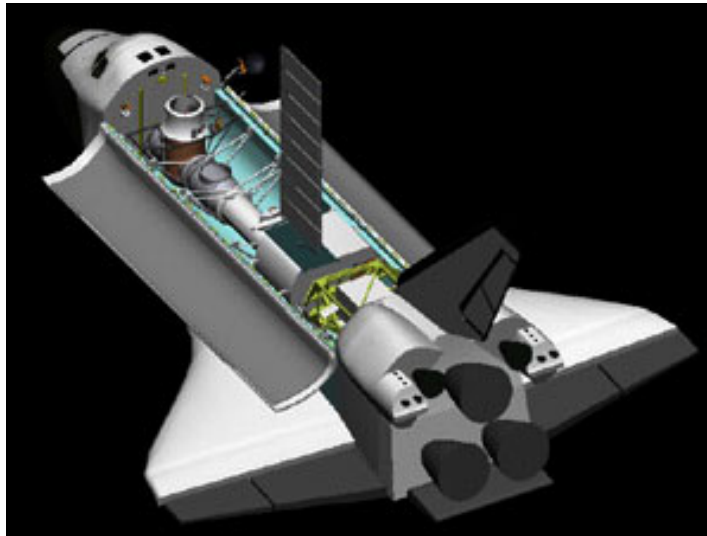


Figure 1 NMP ST-6 Solar Array Concept

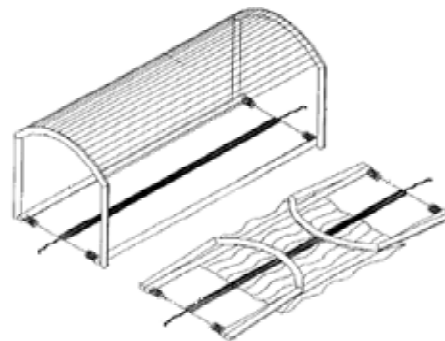


Figure 2 Stretched Lens Element: Deployed and Folded

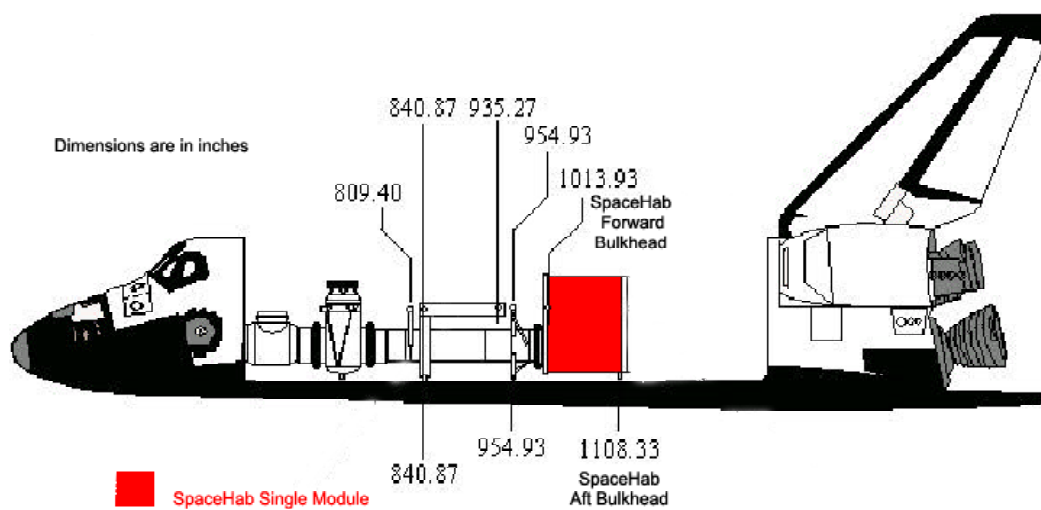


Figure 3 SpaceHab Experiment Platform

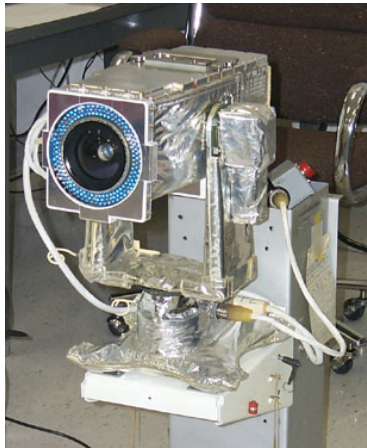


Figure 4 Shuttle Color Television Camera

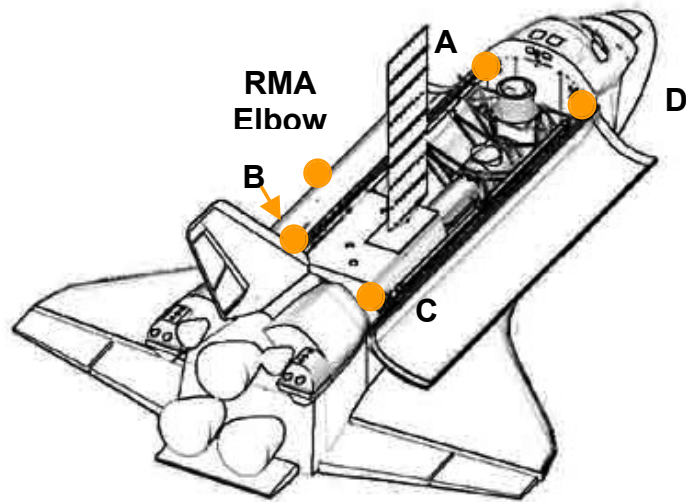
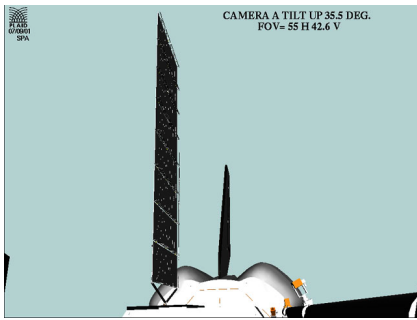
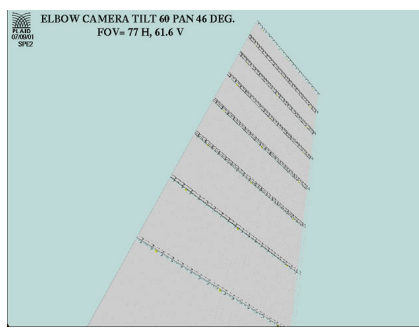


Figure 5 Shuttle Camera Positions for Photogrammetric Simulation

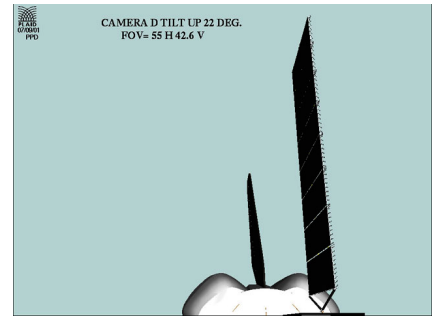
Camera A View



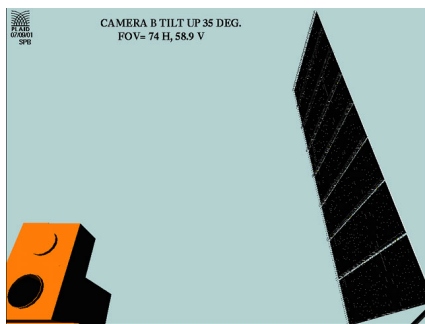
Elbow Camera View



Camera D View



Camera B View



Camera C View

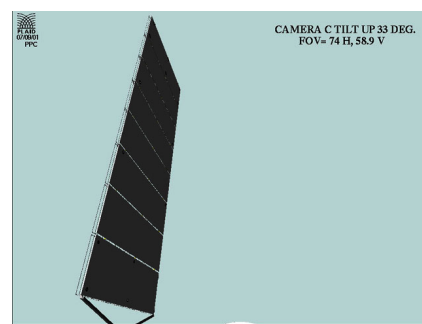


Figure 6 Shuttle camera views from five camera locations for photogrammetric simulation with array plane parallel to X-Axis of Orbiter

Camera B View



Camera C View

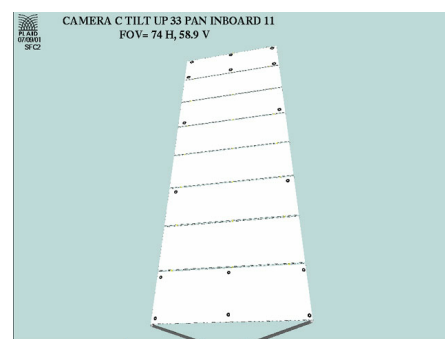


Figure 7 Example camera views from locations B and C with array plane perpendicular to X-Axis of Orbiter

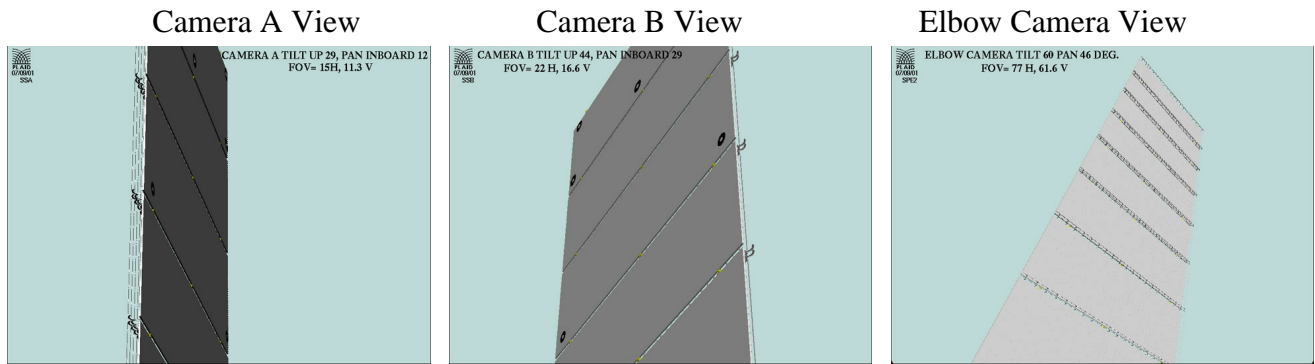


Figure 8 Example close-up views of the top panel from locations A, B and Elbow with array plane parallel to X-Axis of Orbiter and with array on the starboard side of SpaceHab

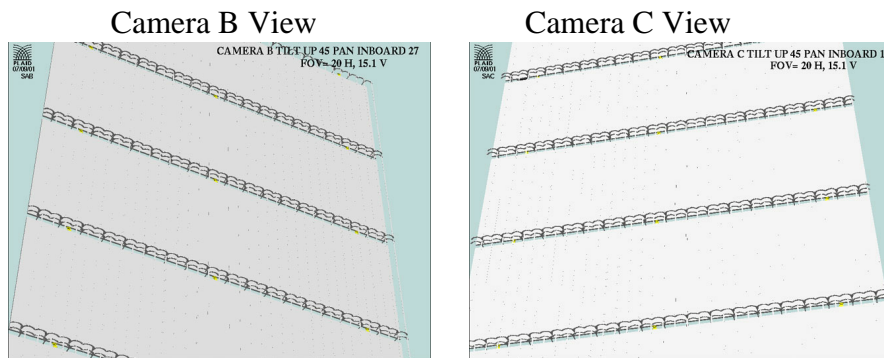


Figure 9 Example close-up views of the top panel from locations B and C with array plane perpendicular to X-Axis of Orbiter and with array on the starboard side of SpaceHab

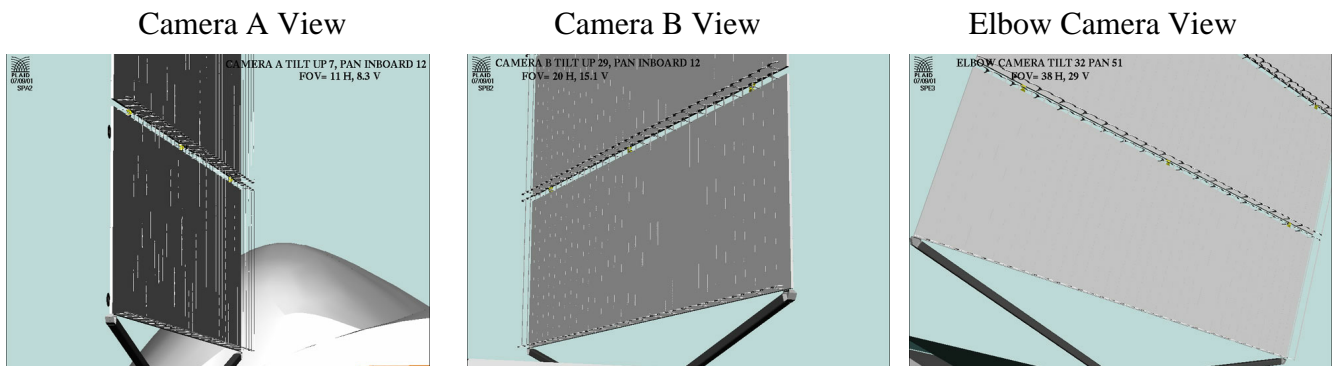


Figure 10 Example close -up views of the bottom panel from locations A, B and Elbow with array plane parallel to X-Axis of Orbiter and with array on the starboard side of SpaceHab

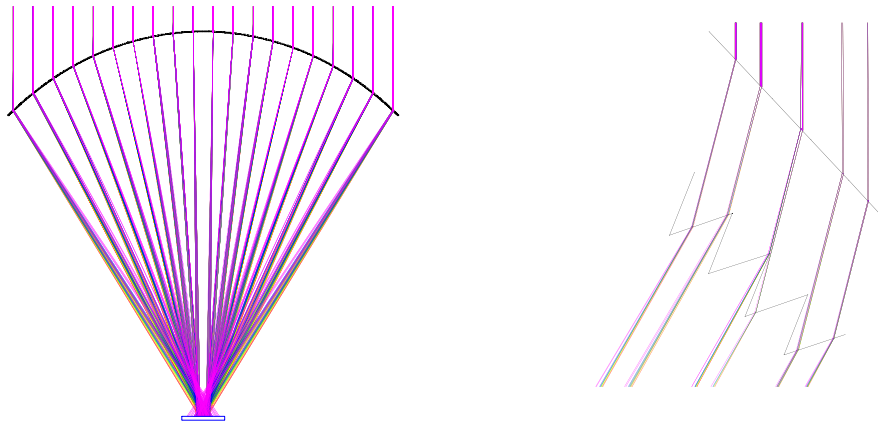


Figure 11 Optical Ray Trace of Lens Element

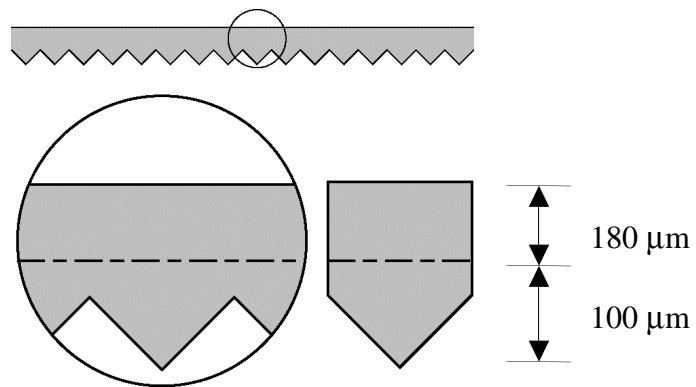


Figure 12 Close-up of Lens Geometry

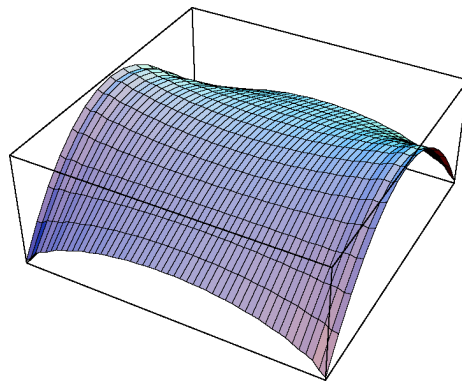


Figure 13 Static lens analysis results showing mid-section flattening
 $(h_a = 229 \mu\text{m}, h_b = 236 \mu\text{m} \text{ and } \epsilon_x = 2\%)$

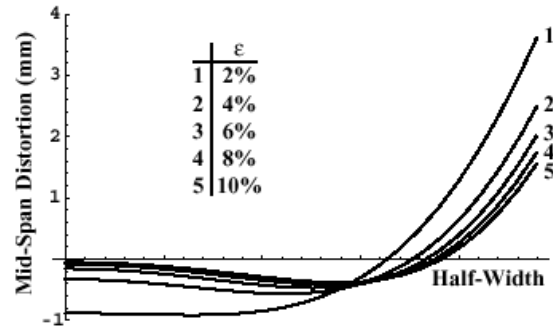


Figure 14 Mid-Span Distortion of a Tensioned Lens as a Function of Strain
($h_a = 229 \mu\text{m}$, $h_b = 236 \mu\text{m}$)

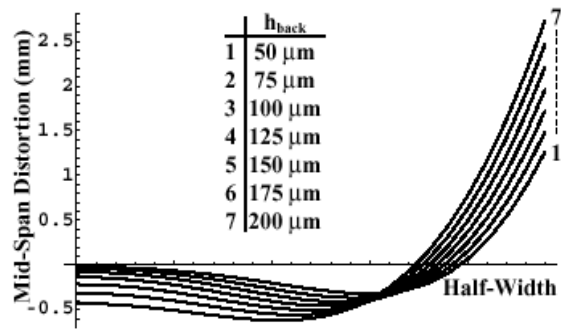


Figure 15 Mid-Span Distortion of a Tensioned Lens as a Function of Lens Thickness
($h_a = 229 \mu\text{m}$ and $\epsilon_x = 2\%$)

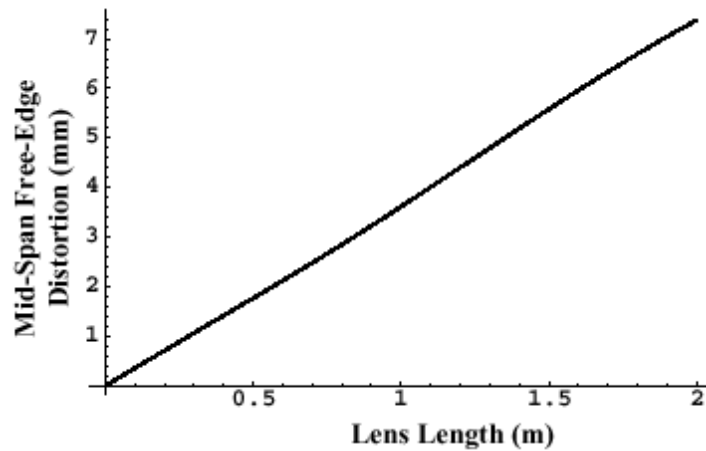


Figure 16 Mid-Span Free-edge Distortion as a Function of Lens Length
($h_a = 229 \mu\text{m}$, $h_b = 236 \mu\text{m}$ and $\epsilon_x = 2\%$)

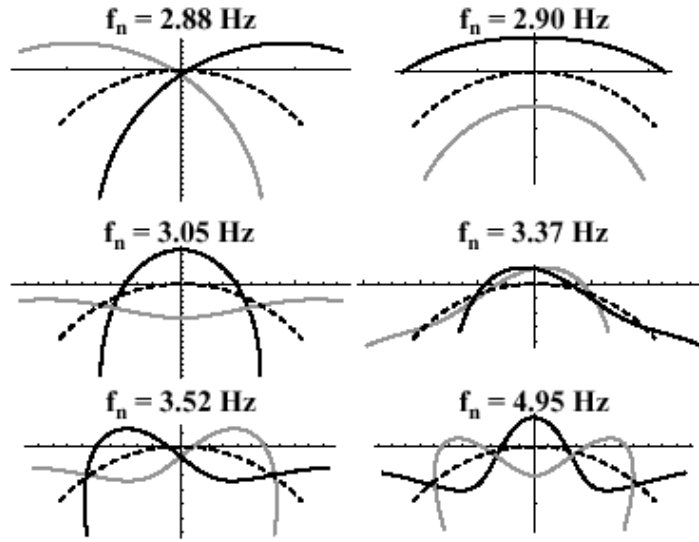


Figure 17 First six longitudinal lens modeshapes from continuous model
($h_a = 150 \mu\text{m}$, $h_b = 150 \mu\text{m}$ and $\varepsilon_x = 2\%$)

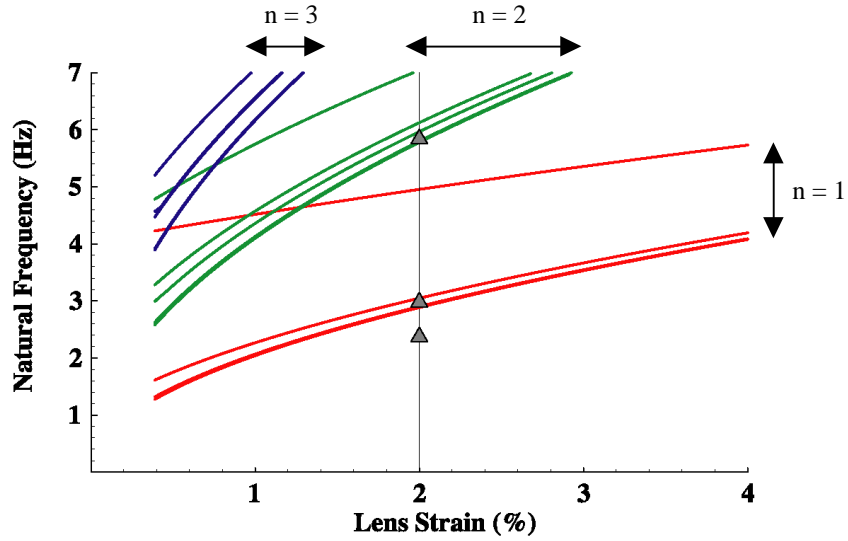


Figure 18 Natural Frequency Variation as a Function of Lens Strain showing
Experimental Data Points ($h_a = h_b = 150 \mu\text{m}$)

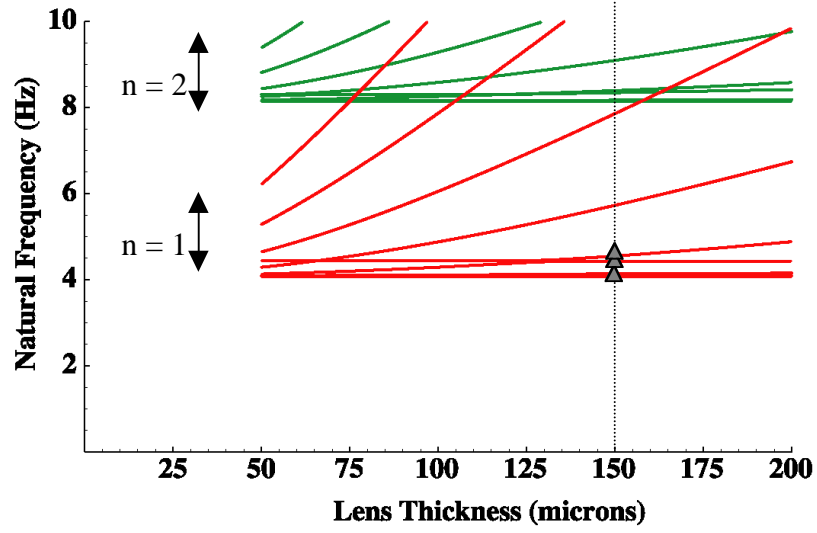


Figure 19 Variation of Natural Frequency as a Function of the Lens Thickness showing Finite Element Analysis Points ($h_a = h_b = 150 \mu\text{m}$ and $\varepsilon_x = 4\%$)

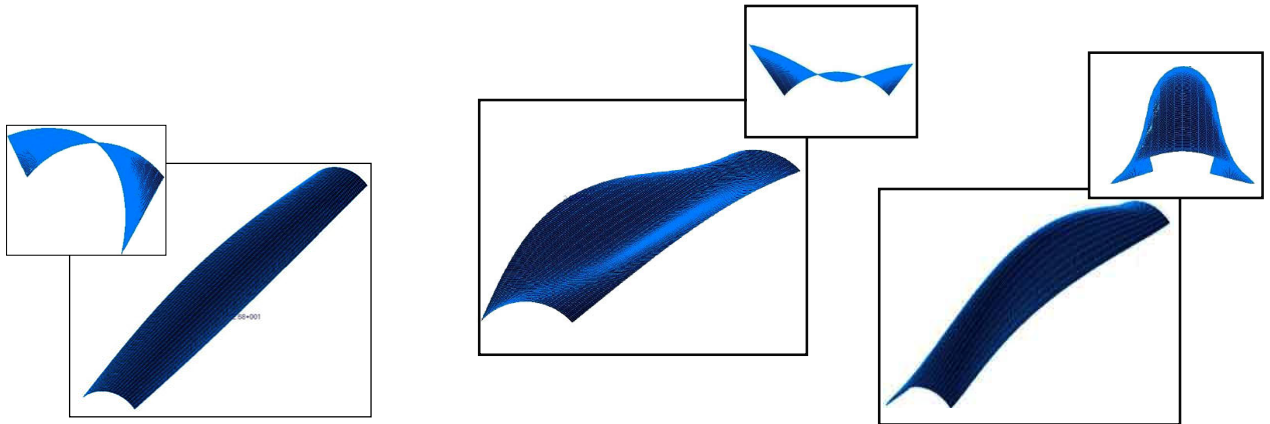


Figure 20 First three lens modeshapes at a) 4.25 Hz b) 4.27 Hz and c) 4.46 Hz ($h_a = h_b = 150 \mu\text{m}$ and $\varepsilon_x = 4\%$)

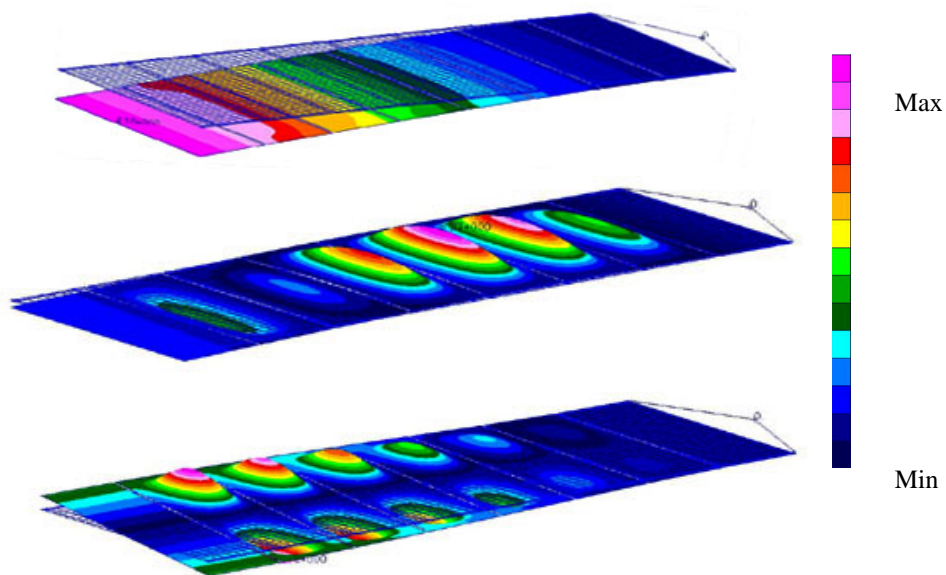


Figure 21 a) 0.1 Hz b) 0.377 Hz c) 0.383 Hz Modeshapes of Array

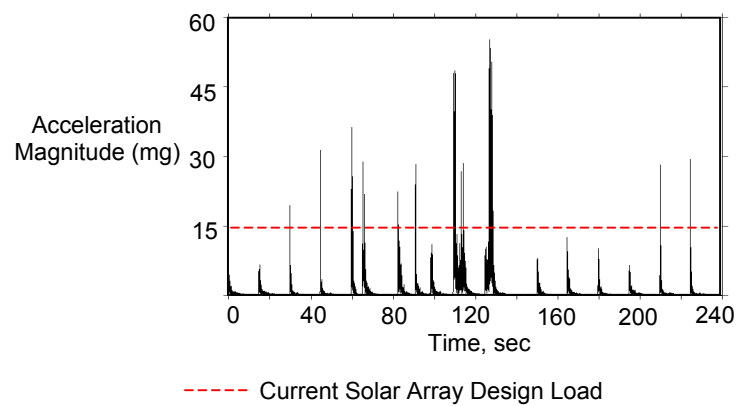


Figure 22 Typical Primary Reaction Control System (PRCS) Response

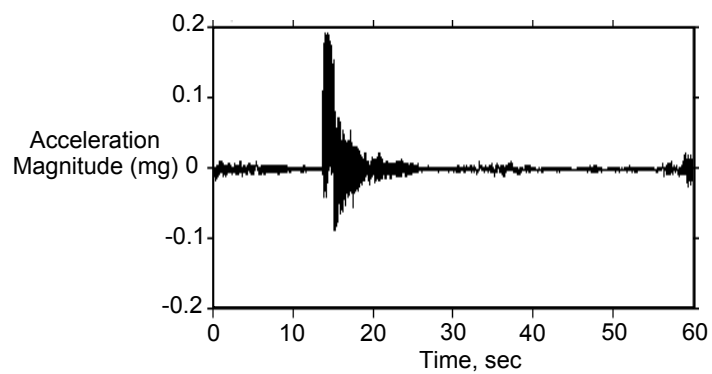


Figure 23 Typical Vernier Reaction Control System (VRCS) Response

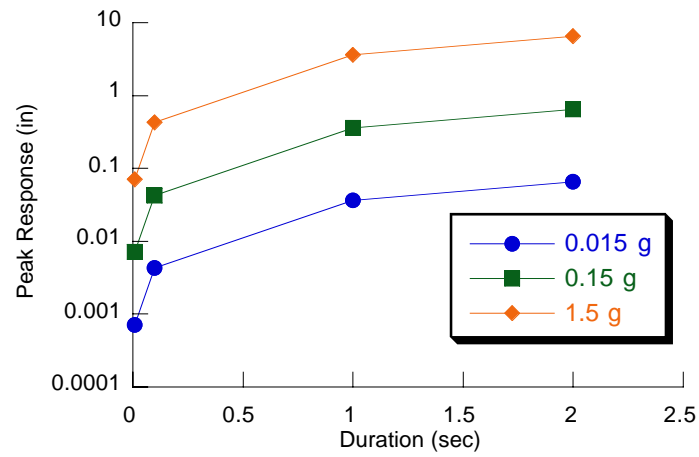


Figure 24 Peak Tip Response due to Single Pulses with Varying Amplitude

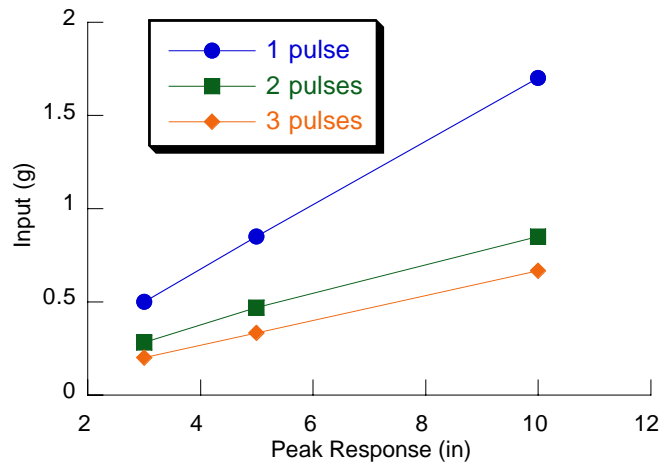


Figure 25 Peak Tip Response due to Multiple Pulses with Varying Amplitude

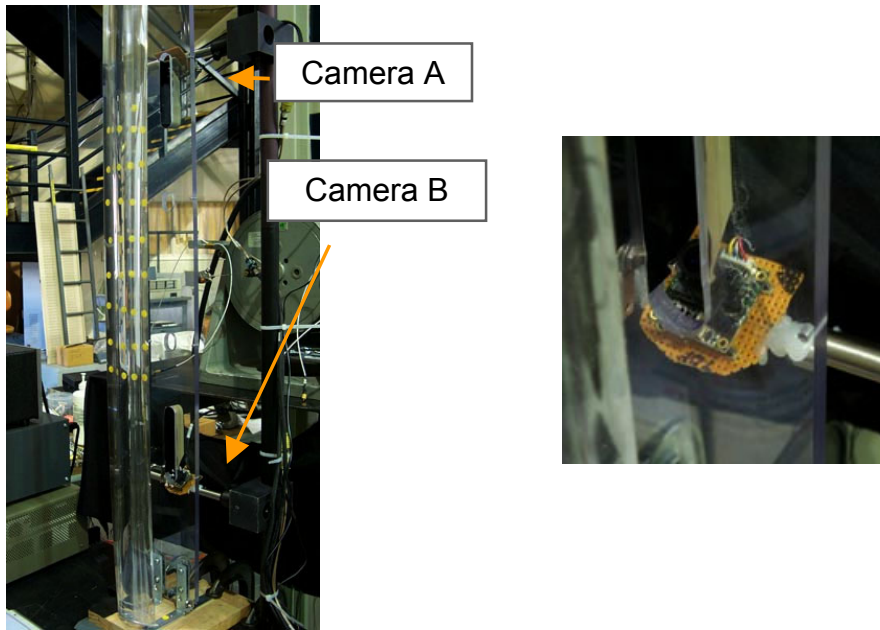


Figure 26 Mini-Cameras Located under 1-meter Stretched Lens

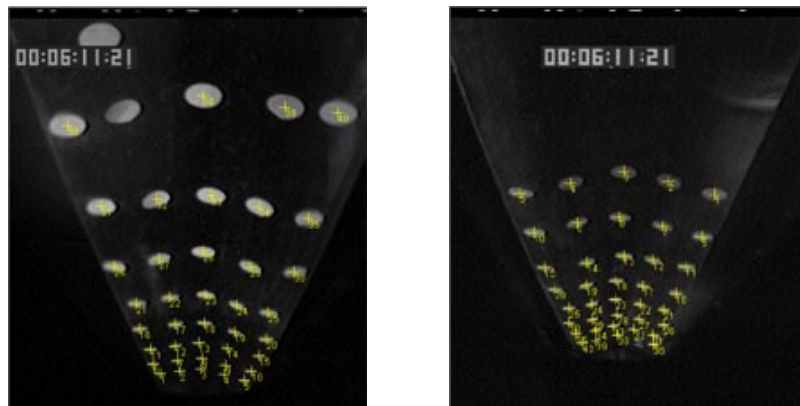


Figure 27 Typical Synchronized Image Pair from Mini-Cameras A and B

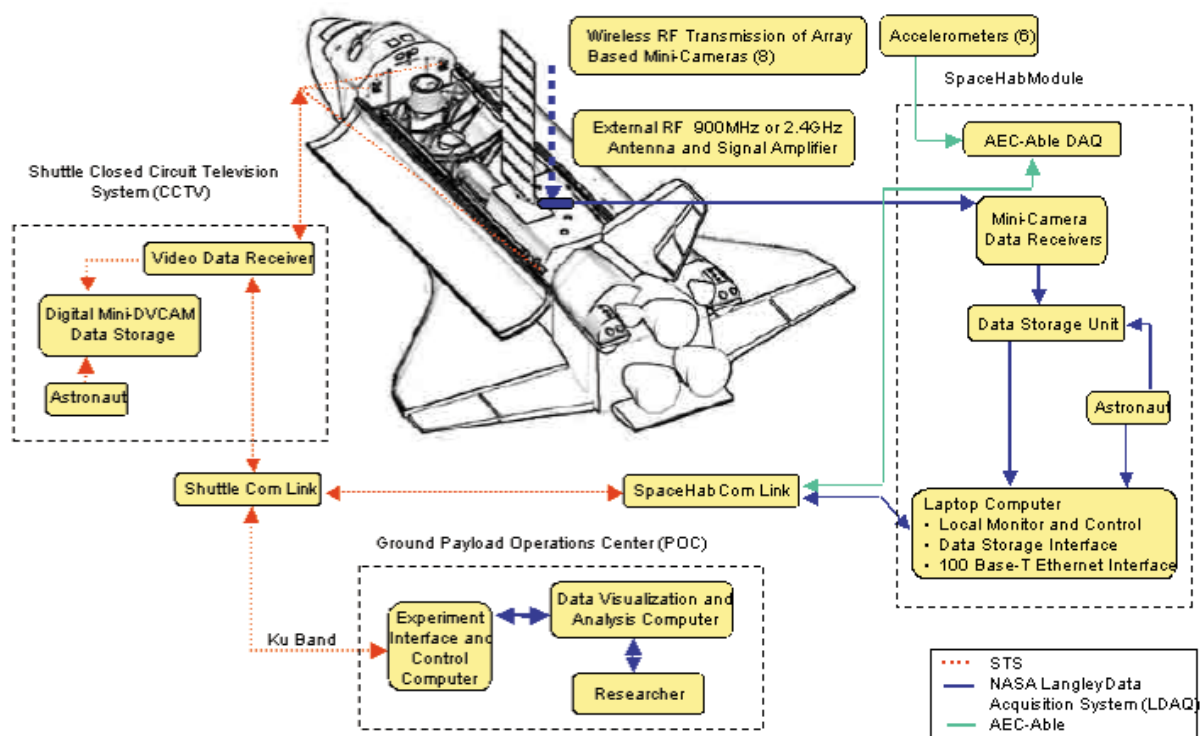


Figure 28 Diagram of Structural Measurement System Concept

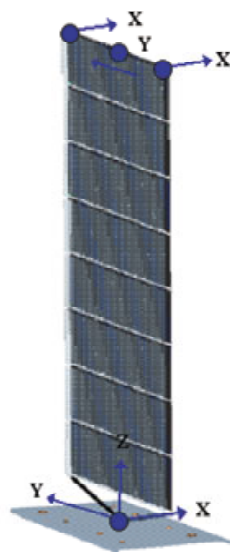


Figure 29 Location of Accelerometers on the Solar Array Test Article.

REPORT DOCUMENTATION PAGE			Form Approved OMB No. 0704-0188	
Public reporting burden for this collection of information is estimated to average 1 hour per response, including the time for reviewing instructions, searching existing data sources, gathering and maintaining the data needed, and completing and reviewing the collection of information. Send comments regarding this burden estimate or any other aspect of this collection of information, including suggestions for reducing this burden, to Washington Headquarters Services, Directorate for Information Operations and Reports, 1215 Jefferson Davis Highway, Suite 1204, Arlington, VA 22202-4302, and to the Office of Management and Budget, Paperwork Reduction Project (0704-0188), Washington, DC 20503.				
1. AGENCY USE ONLY (Leave blank)	2. REPORT DATE March 2002	3. REPORT TYPE AND DATES COVERED Technical Memorandum		
4. TITLE AND SUBTITLE Concept Definition Study for In-Space Structural Characterization of a Lightweight Solar Array: Final Report		5. FUNDING NUMBERS WU 629-60-00-01		
6. AUTHOR(S) Jessica A. Woods-Vedeler, Richard S. Pappa, Thomas W. Jones, Regina Spellman, Willis Scott, Eric M. Mockensturm, Donn Liddle, Ed Oshel, and Michael Snyder				
7. PERFORMING ORGANIZATION NAME(S) AND ADDRESS(ES) NASA Langley Research Center Hampton, VA 23681-2199		8. PERFORMING ORGANIZATION REPORT NUMBER L-18162		
9. SPONSORING/MONITORING AGENCY NAME(S) AND ADDRESS(ES) National Aeronautics and Space Administration Washington, DC 20546-0001		10. SPONSORING/MONITORING AGENCY REPORT NUMBER NASA/TM-2002-211629		
11. SUPPLEMENTARY NOTES				
12a. DISTRIBUTION/AVAILABILITY STATEMENT Unclassified-Unlimited Subject Category 39 Availability: NASA CASI (301) 621-0390		12b. DISTRIBUTION CODE		
13. ABSTRACT (Maximum 200 words) A Concept Definition Study (CDS) was conducted to develop a proposed "Lightweight High-Voltage Stretched-Lens Concentrator Solar Array Experiment" under NASA's New Millennium Program Space Technology-6 (NMP ST-6) activity. As part of a multi-organizational team, NASA Langley Research Center's role in this proposed experiment was to lead Structural Characterization of the solar array during the flight experiment. In support of this role, NASA LaRC participated in the CDS to define an experiment for static, dynamic, and deployment characterization of the array. In this study, NASA LaRC traded state-of-the-art measurement approaches appropriate for an in-space, STS-based flight experiment, provided initial analysis and testing of the lightweight solar array and lens elements, performed a lighting and photogrammetric simulation in conjunction with JSC, and produced an experiment concept definition to meet structural characterization requirements.				
14. SUBJECT TERMS structural dynamics, experiment, space, deployment, membrane, photogrammetry, simulation, solar array, fresnel lens			15. NUMBER OF PAGES 38	
			16. PRICE CODE	
17. SECURITY CLASSIFICATION OF REPORT Unclassified	18. SECURITY CLASSIFICATION OF THIS PAGE Unclassified	19. SECURITY CLASSIFICATION OF ABSTRACT Unclassified	20. LIMITATION OF ABSTRACT UL	